The Astrophysical Journal, 993:184 (19pp), 2025 November 10 https://doi.org/10.3847/1538-4357/ae064a

Binding Energies of Interstellar Complex Organic Molecules on Water Ice Surfaces: A Quantum Chemical Investigation

Harjasnoor Kakkar[1], Berta Martínez-Bachs[1], Cecilia Ceccarelli[2], Piero Ugliengo[3], and Albert Rimola[1]
[1] Departament de Química, Universitat Autònoma de Barcelona, Bellaterra, E-08193, Catalonia, Spain; albert.rimola@uab.cat
[2] Université Grenoble Alpes, CNRS, Institut de Planétologie et d'Astrophysique de Grenoble (IPAG), F-38000 Grenoble, France; cecilia.ceccarelli@univ-grenoble-alpes.fr
[3] Dipartimento di Chimica and Nanostructured Interfaces and Surfaces (NIS) Centre, Università degli Studi di Torino, via P. Giuria 7, I-10125, Torino, Italy
Received 2025 June 13; revised 2025 September 1; accepted 2025 September 10; published 2025 November 3

Abstract

Interstellar dust grains are enveloped by ices of frozen molecules in cold, dense regions of the interstellar medium (ISM), which are also observed in the gas phase. Whether a species is in the solid or gaseous state is governed by its binding energy (BE) on the grains. Hence, BEs are crucial in the solid-to-gas transition and are key input parameters for astrochemical models that simulate the physicochemical processes leading to the evolution of chemistry in the ISM. About 40% of the currently detected interstellar molecules belong to the category of interstellar complex organic molecules (iCOMs). This work aims to accurately evaluate the BEs of 19 iCOMs by means of quantum chemical calculations. Atomistic surface models simulating the structures of both crystalline and amorphous water ice were employed adopting a periodic approach, thereby accounting for the hydrogen bond (H-bond) cooperativity imparted by the extensive network present in the surfaces. A cost-effective but reliable procedure based on density functional theory was used to predict the structures of the adsorption complexes and calculate their BEs, which are mainly driven by H-bond and dispersion interactions, the latter presenting a fair contribution. A final discussion on the astrophysical implications of the computed BEs and the importance of obtaining reliable BEs on realistic interstellar ice surfaces in relation to the snow lines of iCOMs in hot cores/corinos and protoplanetary disks is provided.

Unified Astronomy Thesaurus concepts: Astrochemistry (75); Surface ices (2117); Interstellar dust (836); Interstellar molecules (849); Dense interstellar clouds (371); Interstellar medium (847); Solid matter physics (2090); Interstellar dust processes (838); Computational methods (1965)

1. Introduction

The interstellar medium (ISM) was presumed to be highly unfavorable to chemistry until the detection of the first diatomic species, CH, by near-ultraviolet transitions, in the late 1930s (P. Swings & L. Rosenfeld 1937; A. McKellar 1940). Since then, with the advancement in observational facilities that provide accurate rotational and vibrational lines in the radio to far-infrared wavelengths, the number of interstellar species detected in the gas phase has steadily increased to more than 330 molecules to date (C. P. Endres et al. 2016; B. A. McGuire 2022).

The formation process of a solar-type planetary system has its origins in the "stellar nurseries" or molecular clouds, i.e., cold (∼10 K) and dense (10^4–10^5 cm^{-3}) regions of the ISM. Despite such extreme physical conditions, simple gaseous molecules and nanometer-sized dust grains made of silicates and carbonaceous material are known to be present (A. P. Jones 2016; A. P. Jones et al. 2017), with H_2O frozen on dust grains in the form of enveloping ice mantles (e.g., A. A. Boogert et al. 2015). Other minor components of the ice mantles that have been unambiguously detected in the solid state by near- and mid-infrared observations include volatile molecules such as CO, CO_2, NH_3, CH_3OH, and CH_4 (e.g., A. A. Boogert et al. 2015; M. K. McClure et al. 2023; W. R. M. Rocha et al. 2024), and are hence referred to as "dirty ices."

The comparison of astronomical observations with the laboratory spectra of interstellar ice samples indicates that the ice mantles are most likely present in the amorphous state, specifically in the form of amorphous solid water (ASW; e.g., H. J. Fraser et al. 2004; N. Watanabe & A. Kouchi 2008; T. Hama & N. Watanabe 2013). These icy surfaces assist the chemical evolution of the ISM by promoting interstellar chemistry in multiple ways, mainly by acting as (i) reactant concentrators or suppliers, so the potential reacting species can accrete on the ice surface, where the components of the ice can also act as the reactants of chemical reactions occurring at the surface of the mantles (e.g., A. Rimola et al. 2018; G. Molpeceres & J. Kästner 2021; J. Perrero et al. 2022b; S. Ferrero et al. 2023a, 2024; G. Molpeceres et al. 2024); (ii) chemical catalysts, in which the ice surfaces provide alternative reaction pathways with lower energy barriers (e.g., L. Zamirri et al. 2019; J. Enrique-Romero et al. 2022; J. Perrero et al. 2022b); or (iii) third bodies that can aid in the dissipation of excess energy from the reactions that occur on the surface, hence stabilizing the newly formed products (e.g., S. Pantaleone et al. 2020, 2021; S. Ferrero et al. 2023b; G. Molpeceres et al. 2023). In practice, the physicochemical processes involved in gas-grain surface chemistry, such as the adsorption, diffusion, and desorption of species, all depend on one fundamental parameter: the binding energy (BE) of the molecules with the ice surface.

Among the detected species in the ISM, the so-called interstellar complex organic molecules (iCOMs) occupy a

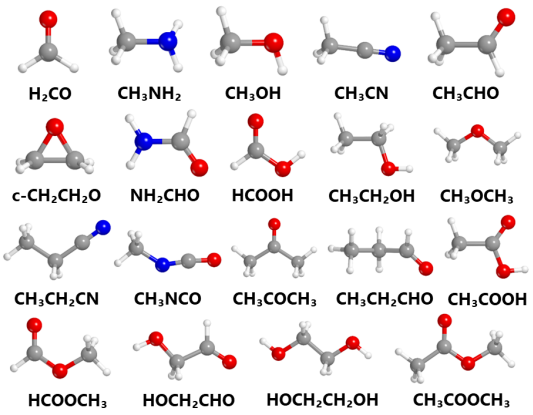

Figure 1. Set of iCOMs considered in this work. Color code: red for oxygen, white for hydrogen, gray for carbon, and blue for nitrogen.

central position, as about 40% of interstellar and circumstellar molecules are iCOMs (C. Ceccarelli et al. 2023). iCOMs are defined as carbon-bearing species containing six or more atoms (E. Herbst & E. F. van Dishoeck 2009; C. Ceccarelli et al. 2017), although some molecules that are excluded from this category still play a vital role in the organic and prebiotic evolution of the ISM (e.g., H_2CO and HCOOH). These compounds are considered to be complex in an astrophysical context, where the largest identified molecule, cyanocoronene, contains 37 atoms at most (so far in only one source, G. Wenzel et al. 2025). Also, the larger the iCOM, the larger the number of rotational transitions and the weaker the intensity of the lines, making them more difficult to identify (C. Ceccarelli et al. 2017).

Yet iCOMs have been detected in numerous high- and low-mass protostars, mostly in hot cores and corinos (e.g., G. A. Blake et al. 1987; S. Cazaux et al. 2003; V. Taquet et al. 2015; A. López-Sepulcre et al. 2017; A. Belloche et al. 2020; E. Bianchi et al. 2020; S. Manigand et al. 2020; M. L. van Gelder et al. 2020; P. Nazari et al. 2021; J.-E. Lee et al. 2023) and protostellar outflows (e.g., R. Bachiller et al. 1995, 1998; H. G. Arce et al. 2008; C. Codella et al. 2017; B. Lefloch et al. 2017; A. López-Sepulcre et al. 2024). More recently, iCOMs have also been detected in cold prestellar cores (e.g., A. Bacmann et al. 2012; J. Cernicharo et al. 2012; S. Scibelli & Y. Shirley 2020; J. Cernicharo et al. 2021; E. Bianchi et al. 2023; M. Agúndez et al. 2025; G. Wenzel et al. 2025).

Finally, in addition to their possible prebiotic role, iCOMs act as an important link between the different phases of stellar evolution, being detected in the early stages of Solar-like forming stars, such as hot corinos, and in the small bodies of the solar system, such as comets (e.g., D. Bockelée-Morvan & N. Biver 2017; E. Bianchi et al. 2019; M. N. Drozdovskaya et al. 2019; M. Lippi et al. 2024).

In this work, we focus on the BEs of the following 17 iCOMs and 2 organic molecules that are precursors of iCOMs, hereafter collectively referred to as iCOMs for convenience (see also Figure 1): formaldehyde (H_2CO), methylamine (CH_3NH_2), methanol (CH_3OH), methyl cyanide (CH_3CN), acetaldehyde (CH_3CHO), ethylene oxide (c-CH_2CH_2O), formamide (NH_2CHO), formic acid (HCOOH), ethanol (CH_3CH_2OH), dimethyl ether (CH_3OCH_3), ethyl cyanide (CH_3CH_2CN), methyl isocyanate (CH_3NCO), acetone (CH_3COCH_3), propanal (CH_3CH_2CHO), acetic acid (CH_3COOH), methyl formate ($HCOOCH_3$), glycolaldehyde ($HOCH_2CHO$), ethylene glycol ($HOCH_2CH_2OH$), and methyl acetate (CH_3COOCH_3). These species were chosen because they are frequently detected in star-forming regions (see the references provided). We report new quantum chemical computations of the BEs of these molecules, following the methodology developed in previous studies from our groups (S. Ferrero et al. 2020; J. Perrero et al. 2022a; B. Martínez-Bachs et al. 2024).

The article is structured as follows. Section 2 briefly reviews the works (experimental and theoretical) related to the BEs of iCOMs available in the literature. Section 3 describes the methods used in this work to derive the BEs of the target iCOMs. Section 4 reports the results obtained by our calculations, and Section 5 discusses the comparison with previous estimates of BEs of the same iCOMs and the astrophysical implications of our newly computed BEs. Section 6 summarizes the major findings of our work.

2. Previous Studies

Several studies have been carried out to determine accurate BEs by means of laboratory experiments and theoretical computations. Experiments utilize the temperature-programmed desorption (TPD) technique to obtain effective BEs (A. Behmard et al. 2019; M. Minissale et al. 2022). This method involves a substrate fixed at a constant temperature, which is first exposed to the adsorbate, and upon adsorption in a certain regime (e.g., sub-monolayer, monolayer, or multilayer), the temperature is increased until the adsorbate is completely removed and analyzed by a mass spectrometer. There are multiple methods to extract the desorption kinetic parameters from TPD spectra by using the Polanyi–Wigner equation (M. Polanyi & E. Wigner 1925; R. Luna et al. 2015; M. Schmid et al. 2023), such as Redhead analysis (P. Redhead 1962; N. F. W. Ligterink & M. Minissale 2023), leading edge analysis (D. A. King 1975; M. P. Collings et al. 2015), and heating rate variation method (V. Rakić & L. Damjanović 2013).

Some experimental studies focusing on the desorption of iCOMs from water ice are available. A. Behmard et al. (2019) investigated the desorption of two to three C-containing hydrocarbons from compact and porous amorphous water ice. They found that BEs on the porous ice are higher than those on the compact ice. In M. Lattelais et al. (2011), the desorption of two sets of isomers, acetic acid/methyl formate and ethanol/dimethyl ether, was observed using a crystalline water ice surface, in which their theoretical simulations were also in agreement with the experimentally obtained BEs. Further studies have examined the structural isomers of $C_2O_2H_4$ (glycolaldehyde, acetic acid, and methyl formate; H. Kaur et al. 2025). D. J. Burke et al. (2014) explored the adsorption and thermal desorption of these three isomers on amorphous water ice, revealing that the presence of water ice strongly influenced their thermal processing behavior. Methyl formate desorbed even at lower temperatures, thereby accounting for its detection in a broad range of physical environments. S. Ferrero et al. (2022) and G. Molpeceres et al. (2022) evaluated the BE of acetaldehyde using both experiment and theory, and obtained a distribution of BEs. They also proposed nonthermal desorption of acetaldehyde to account for its gas-phase detection in the prestellar cores. A similar procedure was performed by J. Perrero et al. (2024b), combining TPD experiments and theoretical calculations for the binding of

ethanol and ethylamine on water ice surfaces. Recently, N. F. W. Ligterink & M. Minissale (2023) compiled the TPD data from past literature with interstellar molecules on different substrates and obtained the BEs using transition state theory (TST) and Redhead analysis. The comparison of some of these experimentally obtained BEs with the present work is discussed in detail in Section 5.1.

While there have been numerous studies on the estimation of BEs using TPD experiments (J. E. Schaff & J. T. Roberts 1998; M. Bertin et al. 2011, 2017; H. Chaabouni et al. 2018; T. L. Salter et al. 2018), there are several limitations of this technique. Some species are highly reactive or unstable (radicals, cyanopolyynes), or toxic (HCN, CH_3NCO) and thus unsuitable for experiments. Consequently, most of the experimental works focus on a handful of astrochemically relevant species. Another drawback is the challenge of accurately simulating the ISM conditions and molecular abundances. Finally, BEs obtained from TPD experiments strongly depend on the morphology of the substrate and the deposition coverage (sub-monolayer, monolayer, or multilayer).

Another alternative to obtaining BEs is by means of computational chemistry approaches, which can overcome experimental limitations in some cases. In this regard, several studies adopted minimal nuclearity water clusters ($[H_2O]_n$, $n = 1$–6) to simulate the ice surface and compute the BEs of relevant interstellar species (e.g., V. Wakelam et al. 2017; A. Das et al. 2018). W. M. C. Sameera et al. (2017) obtained the BEs for OH, CHO, and CH_3 radicals on a large cluster model for crystalline water ice adopting the ONIOM (Our own N-layered Integrated molecular Orbital and Molecular mechanics) approach, using a hybrid QM:MM (quantum mechanics:molecular mechanics) methodology. D. Duflot et al. (2021) computed the BEs of small atoms and molecules on crystalline and amorphous ices represented by a cluster of 150 water molecules. T. Villadsen et al. (2022) employed machine learning to predict BEs for 21 molecules, using the existing literature as the training data set. G. M. Bovolenta et al. (2022) presented BE distributions for 21 interstellar species using different amorphous clusters comprising 22 H_2O molecules. Focusing on accurate atomistic modeling of the amorphous water ice surface, A. Germain et al. (2022) developed a procedure to build icy grains of up to 1000 molecules using the semiempirical GFN2-xTB (Geometries, Frequencies, and Non-covalent interactions eXtended Tight Binding, version 2) level of theory, and computed a distribution of BEs for ammonia as a test case. L. Tinacci et al. (2022) optimized the NH_3 systems obtained by A. Germain et al. (2022) using ONIOM2 (Our own *N*-layered Integrated molecular Orbital and Molecular mechanics, 2-layer scheme) approximations with density functional theory (DFT) methods, and further refinement with a CCSD(T) (Coupled-Cluster with Single, Double, and perturbative Triple excitations) level of theory. Using this methodology, L. Tinacci et al. (2023) evaluated a range of BE for H_2O on a number of adsorption sites on the amorphous ice model. V. Bariosco et al. (2024) obtained a distribution of BEs for H_2S while also employing a pruning procedure to eliminate identical binding sites. A similar procedure was used to obtain a range of BEs for CH_3OH by V. Bariosco et al. (2025). Recently, M. Groyne et al. (2025) obtained BE distributions for NH_3, CH_4, and CO on molecular dynamics-modeled ASW ice (via heat and quench scheme), adopting an ONIOM (DFT:GFN2-xTB) methodology. A comprehensive discussion of some of these studies in the context of our results is presented in Section 5.1.

The aforementioned studies present BEs of species computed on water clusters. Alternatively, a few works have adopted a periodic approach to model the water ice surfaces and elucidate the adsorption processes. S. Ferrero et al. (2020) evaluated the BEs of 21 small mixed molecules on crystalline and amorphous water ice surfaces, thus taking into account the extensive hydrogen bond (H-bond) network present in pure water ice. The crystalline system was smaller and resulted in one or two BEs, whereas the amorphous surface demonstrated a range of BEs due to the presence of distinct adsorption sites. Another similar work by J. Perrero et al. (2022a) presented the BEs of 17 sulfur-containing species on the same periodic ice models. Recently, B. Martínez-Bachs et al. (2024) computed the BEs of 21 nitrogen-bearing compounds adopting the same ice surfaces. For a detailed comparison of the aforementioned studies with the present work, we refer to Section 5. Additionally, J. Perrero et al. (2024a) computed the BEs of pure sulfur S_n species ($n = 1$–8) on the periodic amorphous ice surface.

Computing BEs is a trade-off between the level of theory used for the calculations and accuracy of the model used to simulate the ice surface. As mentioned previously, several theoretical works focused on the binding of small volatile molecules, ions, and radicals to water ice surfaces, but studies of iCOMs are practically missing, owing to the larger size of the molecules and also the ice slab model required for the computations. The present work thus aims to fill this gap.

Given the relevance of iCOMs and BEs in the astrophysical context, we computed the BEs of 19 iCOMs (see Section 1 and Figure 1) by means of quantum chemical calculations. In order to obtain accurate BEs, we have used the same periodic models (crystalline and amorphous) as used by S. Ferrero et al. (2020) to simulate the structure of interstellar ice. On the crystalline surface model, one or two BEs were computed (due to the presence of limited binding sites), while on the amorphous ice surface, we picked eight different binding sites for an unbiased site selection. This allowed us to obtain a range of BEs with values depending on the nature of the site.

3. Methodology

3.1. Computational Details and BE Calculation

The calculations have been carried out in the same manner as in previous similar works (S. Ferrero et al. 2020; J. Perrero et al. 2022a; B. Martínez-Bachs et al. 2024).

The periodic calculations were carried out using the ab initio CRYSTAL17 program (R. Dovesi et al. 2018). This code implements Hartree–Fock and Kohn–Sham self-consistent fields to solve the electronic Schrödinger equation for periodic systems, utilizing the inherent symmetry of the system wherever present. The code employs localized Gaussian functions as basis sets and the local combination of atomic orbitals approximation, a methodology that resembles the approach used in molecular codes. Although plane waves are commonly used for periodic systems (normally used in metallic systems presenting electron delocalization), here we use Gaussian-type orbitals (GTOs) centered on atoms as they allow using hybrid DFT methods, which provide a very good description of electron-localized H-bonded molecular

solid-state systems (B. Civalleri et al. 2007), like water ice. Moreover, hybrid functionals are essential for accurately describing adsorption complexes driven by H-bonding and are more computationally efficient with GTOs, especially in surface models where large vacuum regions would otherwise be required.

For the crystalline ice model, the hybrid DFT functional, B3LYP (C. Lee et al. 1988; A. D. Becke 1993), in conjunction with Grimme's D3 empirical correction within the Becke–Johnson (BJ) damping scheme to introduce dispersion interactions (S. Grimme et al. 2010; S. Grimme 2011; R. Sure & S. Grimme 2013), i.e., the B3LYP-D3(BJ) method, was used in the geometry optimization for the adsorption of the iCOMs. This method was combined with the Ahlrichs triple-zeta valence quality basis set complemented with a double set of polarization functions, i.e., A-TVZ* (A. Schäfer et al. 1992). This full DFT treatment is hereafter referred to as DFT//DFT.

All the adsorption complexes on the crystalline surface were characterized by calculating their harmonic frequencies. In CRYSTAL, this is done numerically at the Γ point by diagonalizing the mass-weighted Hessian matrix of the second-order energy derivatives with respect to atom displacements (central difference formula), in this case of ±0.003 Å from the minimum along each Cartesian coordinate (F. Pascale et al. 2004; C. M. Zicovich-Wilson et al. 2004). To save computational time, the Hessian matrix was only computed for a fragment of the system, which includes the iCOM and the minimum number of water molecules (i.e., those directly interacting with the iCOM) in direct contact with the iCOM. Despite computing a Hessian matrix fragment, the electronic Hamiltonian includes the whole system—that is, the energy variation and the corresponding gradient due to nuclear displacements within the fragment account for contributions from the entire system.

Due to the use of a finite basis set, the interaction energies were *a posteriori* corrected for the basis set superposition error (BSSE) using the counterpoise correction (CP) method devised by S. Boys & F. Bernardi (1970),

$$\Delta E^{\mathrm{CP}} = \Delta E - \mathrm{BSSE}, \tag{1}$$

where ΔE is the interaction energy and ΔE^{CP} is the BSSE-corrected interaction energy using the CP scheme. The BSSE-corrected BE considering purely the electronic and dispersion contributions ($\mathrm{BE_{ED}}$) is defined as ΔE^{CP} of opposite sign:

$$\mathrm{BE_{ED}} = -\Delta E^{\mathrm{CP}}. \tag{2}$$

Finally, vibrational zero-point energy (ZPE) corrections were obtained for each structure from their harmonic frequency calculations (as noted previously). The contribution of the ZPE to the binding energies (ΔZPE) was then added to $\mathrm{BE_{ED}}$ to obtain the final BE:

$$\mathrm{BE} = \mathrm{BE_{ED}} - \Delta\mathrm{ZPE}. \tag{3}$$

The complete set of equations used for the computation of the final BEs is detailed in Appendix A.

To confirm the accuracy of the DFT//DFT method, a refinement at the CCSD(T) level was introduced using the Gaussian16 software package (M. J. Frisch et al. 2016) by employing the ONIOM2 approximation (S. Dapprich et al. 1999). The T. H. J. Dunning (1989) correlation consistent family of cc-pVnZ basis sets (where n is 2, 3, 4, ..., corresponding to a D, T, Q, ... zeta basis set) was employed. An extrapolation to the complete basis set limit was then extended by plotting the BE against $1/n^3$. The Jun-cc-pVnZ (with $n = 2$, 3, and 4) basis set was employed to perform the computations (E. Papajak et al. 2011). For this ONIOM2 approach, the adsorbate and directly interacting water molecules were considered as the model system included in the CCSD(T) level calculations, while the rest (real system) was computed at the B3LYP-D3(BJ) level. Within this ONIOM2 scheme (hereafter referred to as O[CCSD(T)//DFT]), the BE(O[CCSD(T)//DFT]) values were calculated as

$$\begin{aligned}\mathrm{BE(O[CCSD(T)//DFT])} &= \mathrm{BE(low, real)} + \mathrm{BE(high, model)},\\ &\quad - \mathrm{BE(low, model)}\end{aligned} \tag{4}$$

where BE(low, real) stands for the BE of the whole periodic (real) system at the low theory level (DFT), and BE(high, model) and BE(low, model) stand for the BEs of the molecular (model) system at the high (CCSD(T)) and low (DFT) theory levels, respectively. The BE terms in Equation (4) were also corrected for BSSE.

Geometry optimization of the iCOMs adsorption on the amorphous ice surface model is almost impractical with the DFT//DFT scheme due to the large number of atoms present in the system. Therefore, the computationally cheaper HF-3c (Hartree–Fock with 3 Corrections) method was adopted (R. Sure & S. Grimme 2013). HF-3c utilizes a minimal basis set (referred to as MINI-1 [H. Tatewaki & S. Huzinaga 1980]), to which three empirical corrections (3c) are added *a posteriori*: (i) the D3(BJ) dispersion contribution for noncovalent interactions, (ii) a short-range bond length correction to rectify the systematically overestimated bond lengths due to the MINI-1 basis set, and (iii) the geometrical CP method developed by H. Kruse & S. Grimme (2012) to remove the BSSE.

To refine the energies, on the optimized HF-3c structures, single-point energy calculations were carried out to compute $\mathrm{BE_{ED}}$s using the same B3LYP-D3(BJ)/A-TVZ* level of theory used for the crystalline complexes, which were also corrected for BSSE. This methodology is hereafter referred to as DFT//HF-3c. Before applying the DFT//HF-3c scheme to the amorphous complexes, its accuracy was checked by comparing it with the full DFT//DFT treatment for the crystalline cases, which resulted in a good correlation.

For frequency calculations in the amorphous adsorption complexes, as they were computed at the approximated HF-3c theory level, the complete systems were considered to build the Hessian matrix. However, due to the inaccuracies of HF-3c regarding the frequencies, here they were only used to confirm that the adsorption complexes are minima on the potential energy surfaces. We instead obtained the ZPE-corrected BE values by applying a scaling factor to the $\mathrm{BE_{ED}}$, which was derived from the DFT//DFT-computed frequencies for the crystalline ice cases. More details regarding the ZPE corrections are provided in Appendix A.

3.2. Water Ice Models

Interstellar ices are mostly dominated by H_2O, while other simple volatile species such as CO, CO_2, NH_3, and CH_3OH are present in minor amounts. In this work, for the sake of

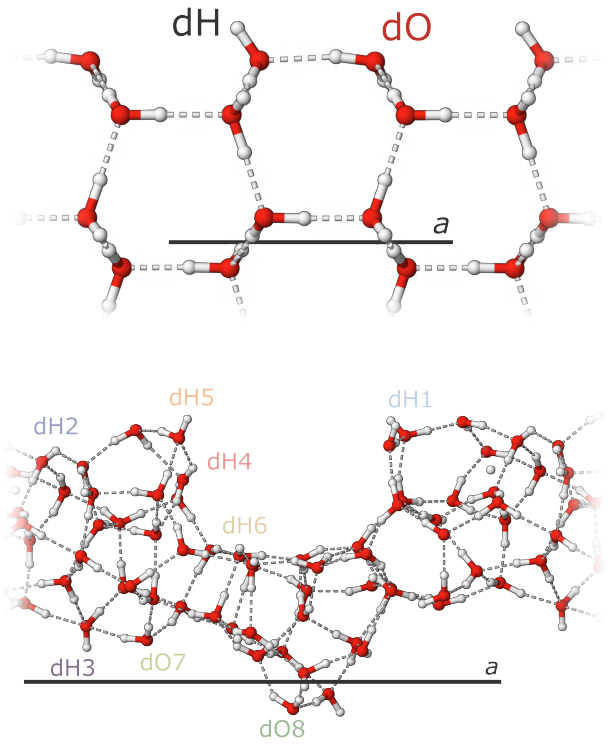

Figure 2. Top panel: side view of the crystalline water (010) P-ice surface model, showing the dangling hydrogen (dH) and oxygen (dO) atoms. Bottom panel: side view of the amorphous water ice surface model, with the labels identifying the different dangling hydrogen (dH) and oxygen (dO) adsorption sites, marked as dH(1–6) and dO(7–8), respectively.

foregoing additional complexity, the ice models were composed of purely water molecules.

A crystalline ice surface was chosen as the starting point (see the top panel of Figure 2), primarily because its well-defined structure, dictated by symmetry constraints, ensures computational efficiency. This makes it suitable for adopting the supercell strategy if an enlargement of the unit cell is required. Notably, certain regions in the stellar outflows and protoplanetary disks have shown the presence of crystalline ice (S. Molinari et al. 1999; M. M. Maldoni et al. 2003). The ice model used in this work was obtained from the bulk of the proton-ordered hexagonal P-ice, which was cut along the (010) plane to generate the corresponding 2D periodic slab model. The reason to choose a proton-ordered model is that the non-proton-ordered model I_h ice would be computationally unfeasible, as the unit cell would need to be sufficiently large to adequately represent the local environment of each water molecule. For crystalline ice, it is crucial to account for long-range H-bond cooperativity and ensure a zero-dipole moment across the slab models, two features that are present in the P-ice model. A (010) P-ice slab model with a thickness of 10.9 Å was sufficient for the convergence of the corresponding surface energy. A 2×1 supercell slab model composed of 24 water molecules was adopted, consisting of 12 atomic layers with optimized lattice parameters at B3LYP-D3(BJ)/A-VTZ* of $|a| = 8.981$ Å and $|b| = 7.082$ Å. For a realistic simulation of the adsorption complexes, utilizing the 2×1 supercell ensures that there are no lateral interactions between adsorbed molecules present in adjacent cells. The crystalline cell shown in Figure 2 presents, on one side of the surface, one dangling hydrogen (dH) atom and one dangling oxygen (dO) atom (per unit cell) as potential binding sites. The ice structure is such that there is no net electric dipole moment along the nonperiodic z-direction. This is the result of the symmetry of the system, which is identical at the top and bottom of the slab model. Hence, the adsorption was simulated only at the top surface of the system.

As mentioned in the introduction to this paper, the majority of ice in the ISM likely exists in an amorphous state (so-called amorphous solid water, or ASW). Thus, we also used a larger, more realistic amorphous ice surface model, which has already been used in previous works (S. Ferrero et al. 2020; J. Perrero et al. 2022a; B. Martínez-Bachs et al. 2024). It is composed of 60 water molecules per unit cell, and it is significantly more extensive compared to the crystalline surface in order to account for the structural variability and lack of orderliness, due to its amorphous nature. The optimized cell parameters at HF-3c are $|a| = 20.353$ Å, $|b| = 10.028$ Å, and $|\gamma| = 103.^{\circ}0$. Due to the lack of symmetry in the top and bottom parts of the amorphous structure, a small electric dipole moment of 1.6 D exists. The lack of long-range order in the ice surface gives rise to a variety of adsorption sites. In order to accurately model the interaction of iCOMs with the ice surface, eight different binding sites were chosen (labeled in the bottom panel of Figure 2): 1–6 sites, which are dangling H atoms (dH), and 7–8 sites, which are dangling O atoms (dO). Sites 1, 2, and 5 are present on the top surface of the structure; sites 4 and 6 are located inside the cavity; while sites 3, 7, and 8 are positioned at the bottom surface of the ice model.

3.3. Calculation of the Desorption Rate Preexponential Factor

In TPD experiments, the BE of an adsorbate on a given substrate is obtained using the first-order Polanyi–Wigner equation (K. W. Kolasinski 2012), where the desorption rate constant $k_{\rm des}(T)$ is written as

$$k_{\rm des}(T) \simeq \nu(T) e^{-{\rm BE}/k_{\rm B}T}, \tag{5}$$

where $\nu(T)$ is the desorption rate preexponential factor (with units of s^{-1}), k_B is the Boltzmann constant, and T is the temperature. Hence, obtaining accurate BE values depends on the accuracy of the $\nu(T)$ used in the equation.

Recent studies (N. F. W. Ligterink & M. Minissale 2023; B. Martínez-Bachs et al. 2024) have employed the following formula derived from the TST for the determination of $\nu_{\rm TST}$ based on S. L. Tait et al. (2005):

$$\nu_{\rm TST} = \frac{k_B T_{\rm peak}}{h} \cdot q^{\ddagger}_{tr,2D} \cdot q^{\ddagger}_{{\rm rot},3D}, \tag{6}$$

where h is the Planck constant; $T_{\rm peak}$ is the experimental peak temperature of the desorption profile in the sub-monolayer regime, which is defined as the temperature at which the TPD spectra exhibit the maximum desorption rate; and $q^{\ddagger}_{tr,2D}$ and $q^{\ddagger}_{{\rm rot},3D}$ represent the 2D translational partition function and the 3D rotational partition function, respectively.

The 2D translational partition function is given by

$$q^{\ddagger}_{tr,2D} = \frac{2\pi m k_{\rm B} T_{\rm peak}}{h^2} A, \tag{7}$$

where m is the mass of the molecule and A is the surface area per adsorbed molecule computed using the unit cell parameters of the crystalline and amorphous ice models (i.e., $A = |a||b|$).

Table 1
Computed Binding Energies without ZPE Corrections (BE_{ED} values) of iCOMs on the Crystalline Water Ice Surface Model

Species	DFT//DFT			DFT//HF-3c			O[CCSD(T)//DFT]
	BE_{ED}	Elec	Disp (%)	BE_{ED}	Elec	Disp (%)	
H_2CO	5869/6375	3885/3692	1985(34)/2682(42)	5773/6423	4053/3716	2369(37)/2057(36)	6575
CH_3NH_2	8455	5537	2918(35)	8498	5438	3060(36)	8167
CH_3OH	8684	6014	2670(31)	8648	6413	2235(27)	8602
CH_3CN	7551	4461	3090(41)	7090	3717	3373(48)	7532
CH_3CHO	6884	3488	3396(49)	5244*/7088	2736*/4568	2508*(48)/2520(36)	6947
c-CH_2CH_2O	6379	3486	2893(45)	5571	2977	2594(47)	6484
NH_2CHO	10079	6483	3608(36)	9634	6074	3560(37)	9638
CH_3CH_2OH	6189	3476	2713(44)	4842*/6106	2070*/3460	2772*(57)/2646(43)	5868
HCOOH	8665	5485	3180(37)	7979	4588	3391(42)	8214
CH_3OCH_3	5532	2483	3049(55)	5471	2812	2659(49)	5510
CH_3CH_2CN	7495	4007	3488(47)	6648	2773	3875(58)	6925
CH_3NCO	5766	2814	2952(51)	6017	2951	3066(51)	5997
CH_3COCH_3	7780	3853	3927(50)	7179	3203	3976(55)	7737
CH_3CH_2CHO	6891	3238	3653(53)	5838*/6922	2719*/3262	3119*(53)/3660(53)	6898
CH_3COOH	10196	6130	4066(40)	9206	7166	2040(22)	10016
$HCOOCH_3$	5799	2987	2812(48)	5641	2752	2889(51)	6020
$HOCH_2CHO$	9717	6187	3530(36)	8430*/8970	5743*/5821	2687*(32)/3149(35)	9534
$HOCH_2CH_2OH$	9653	5330	4323(45)	7985*/9528	4752*/6473	3233*(40)/3055(32)	9332
CH_3COOCH_3	6900	2948	3952(57)	5282*/6648	2783*/2560	2499*(47)/4088(61)	6723

Note. The first column refers to the iCOMs. Columns (2)–(4) report the values computed at the DFT//DFT level of theory. Columns (5)–(7) contain the values computed at the DFT//HF-3c level of theory, and the last column lists the values computed using the CCSD(T) level within the ONIOM2 scheme. The BE contributions arising from the electronic (Elec) and dispersive (Disp) interactions, along with their percentage, are tabulated. The energies are given in K. DFT//HF-3c values marked with asterisks (∗) indicate different adsorption geometries compared to the DFT//DFT optimized structures.

The 3D rotational partition function is given by

$$q^{\ddagger}_{\mathrm{rot},3D} = \frac{\sqrt{\pi}}{\sigma h^3} \cdot (8\pi^2 k_B T_{\mathrm{peak}})^{3/2} \cdot \sqrt{I_x I_y I_z}\,, \tag{8}$$

where σ is the symmetry number that indicates the number of indistinguishable orientations of the molecule, and I_x, I_y, and I_z are the principal moments of inertia for the rotation of the molecule.

4. Results

In this work, the adsorption of 19 closed-shell iCOMs (shown in Figure 1) has been simulated. All the species were manually deposited on the target binding sites (labeled in Figure 2) of the ice surface models, and geometry optimizations were carried out from these initial guess structures.

4.1. Binding Energies on the Crystalline Water Ice Model

4.1.1. DFT//DFT Binding Energies

The computed ZPE-non-corrected BE_{ED} values for the iCOMs on the crystalline water ice surface model are listed in Table 1. For each structure, BE_{ED} is divided into the purely electronic, nondispersive component ("Elec" term, provided by the B3LYP method) and the dispersion component ("Disp" term, imparted by the D3(BJ) correction). This decomposition allows highlighting the importance of the dispersive forces in the BE, which spans a range of 31–57%.

At DFT//DFT, the computed BE_{ED} values range from 5500 to 10,200 K, in which the dispersion contribution (Disp values in Table 1) lies between 2000 and 4400 K. Clearly, BE_{ED} depends on the kind of interaction between the adsorbate and the ice surface, such as H-bonds, interactions among permanent and instantaneous dipole moments, as well as dispersion.

From a chemical perspective, the functional groups of the iCOMs determine their interactions with the ice surface. Molecules possessing a carboxylic (–COOH) group (i.e., HCOOH and CH_3COOH) or a hydroxyl (–OH) group (i.e., CH_3OH, $HOCH_2CH_2OH$, and $HOCH_2CHO$) tend to have high BE_{ED} values due to their ability to establish multiple H-bonds acting as both acceptors and donors. In contrast, species that contain an ester (RCOOR') group (i.e., $HCOOCH_3$ and CH_3COOCH_3), a carbonyl (–CO–) group (i.e., H_2CO, CH_3CHO, CH_3CH_2CHO, and CH_3COCH_3), or an ether (–O–) group (i.e., CH_3OCH_3 and c-CH_2CH_2O) are only capable of acting as H-bond acceptors and consistently exhibit lower BE_{ED} values, in which (in general) the electronic and dispersion terms contribute similarly to the total BE_{ED}. For N-containing iCOMs, CH_3CN, CH_3CH_2CN, and CH_3NCO only act as H-bond acceptors, while NH_2CHO and CH_3NH_2 are both H-bond donors and acceptors.

According to the distribution, acetic acid (CH_3COOH) presents the highest BE_{ED} value (10,196 K). In this case, the electronic contribution (namely that arising from the pure B3LYP method, without the dispersion contribution) is very favorable (6130 K) since the molecule establishes three strong H-bonds as donor and acceptor. Formamide (NH_2CHO), glycolaldehyde ($HOCH_2CHO$), and ethylene glycol ($HOCH_2CH_2OH$) also present high BE_{ED} values. This is because their functional groups (–NH_2, –OH, and –CHO) impart the capability to act as both H-bond donors and acceptors, hence presenting very favorable electronic contributions to the BE_{ED}.

The ZPE corrections involve the computation of harmonic frequencies of iCOMs on the crystalline ice surface. It is

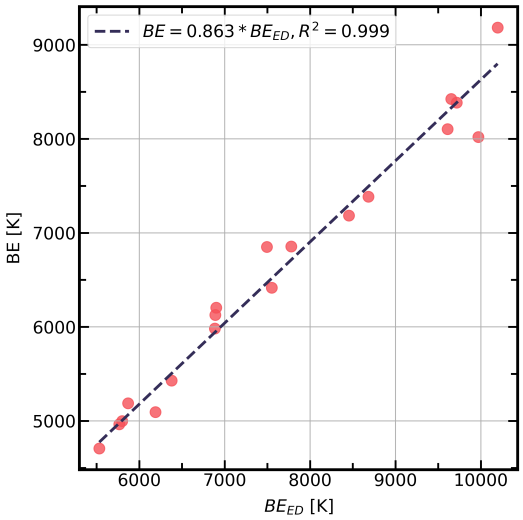

Figure 3. Correlation between DFT//DFT BE_{ED} and ZPE-corrected BE for the adsorption of iCOMs on crystalline ice. The BEs are given in Kelvin. The intercept is set to zero.

assumed that the deformation of the ice structure mainly occurs in the vicinity of the adsorption site. Therefore, in addition to the iCOMs, the directly interacting water molecules are assumed to contribute to ZPE corrections. The correlation between BE_{ED} and the ZPE-corrected BE is plotted in Figure 3, which shows a very good correlation, with a conversion factor of 0.863. This value is applied as a scaling factor to systematically convert BE_{ED} into BE for iCOMs adsorption on the amorphous water ice surface model. Recently, A. Bulik et al. (2025) computed ZPE-corrected BEs with full B3LYP-D3(BJ) treatment and compared them to those from S. Ferrero et al. (2022), who used the hybrid DFT//HF-3c method, as in our work. Results indicated that for H-bonded adsorption complexes (like those present in our work), using a scaling factor to derive ZPE-corrected BEs is actually a fair cost-effective approximation, with errors within 10% at the most.

4.1.2. ONIOM2 Binding Energies

The BE_{ED} values computed at the DFT//DFT level of theory have been refined at a CCSD(T) level using the ONIOM2 scheme explained previously (see Section 3.1). It is based on the assumption that most of the BE is contributed by the interaction between the adsorbate and the neighboring water molecules; hence, the interaction of this "model" system is described at a higher CCSD(T) level. Figure 4(a) shows the plot of the BE_{ED} values computed using the ONIOM2 methodology against those at DFT//DFT, which indicates an excellent correlation between them, confirming the reliability of the DFT//DFT method used for the adsorption of iCOMs on crystalline water ice surface.

4.1.3. DFT//HF-3c Binding Energies

In order to assess the reliability of the DFT//HF-3c methodology to be used for the larger amorphous water ice model, this computationally cheaper scheme has been performed on the crystalline ice model to test its accuracy with respect to DFT//DFT and ONIOM2 BE_{ED} values. To

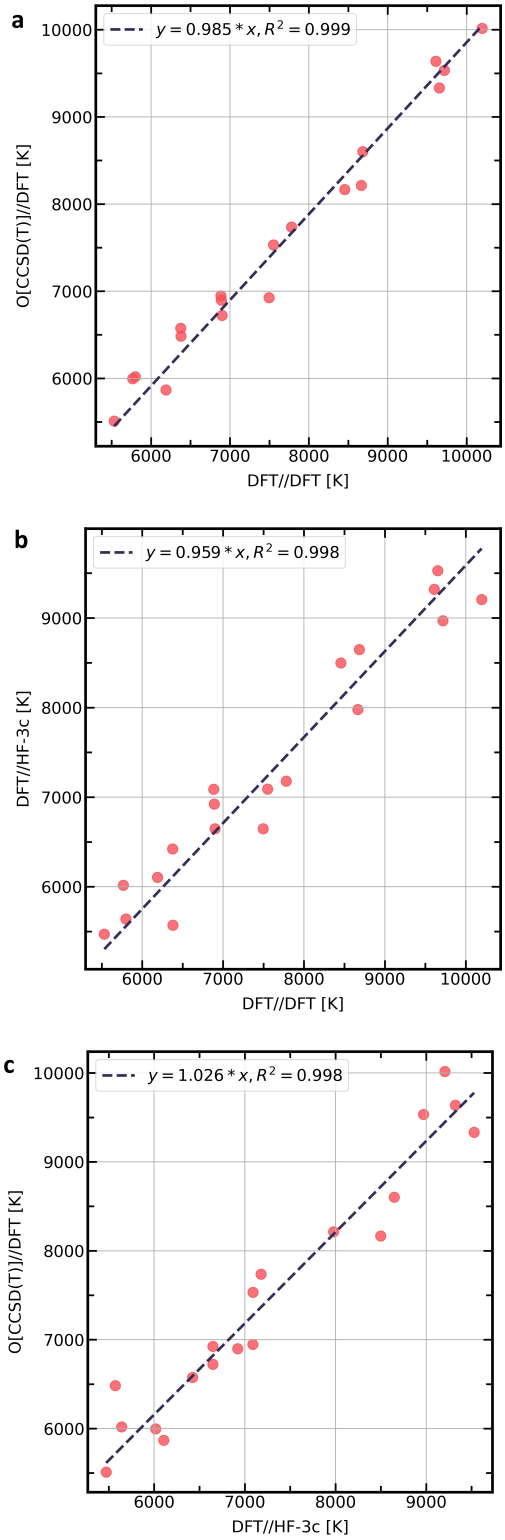

Figure 4. Correlation between (a) DFT//DFT and ONIOM2-corrected CCSD (T) BE_{ED}, (b) DFT//DFT and DFT//HF-3c BE_{ED}, and (c) DFT//HF-3c and ONIOM2-corrected CCSD(T) BE_{ED} for the adsorption of iCOMs on crystalline ice. The BE_{ED} values are given in Kelvin. The intercept is set to zero.

this end, the systems of adsorbed species on the crystalline water ice surface were optimized at the HF-3c level of theory, and single-point energy calculations were then carried out at

Species	dH1	dH2	dH3	dH4	dH5	dH6	dO7	dO8	<BE> ± std
H_2CO	3103	3675	3602	4121	4546	3965	3342	6259	4077 ± 927
CH_3NH_2	5850	5737	6136	7040	4441	8423	6243	5118	6124 ± 1130
CH_3OH	5636	3809	5626	5490	4495	5750	4754	8709	5534 ± 1361
CH_3CN	4997	6517	4396	7696	4716	7703	2665	3477	5271 ± 1750
CH_3CHO	4829	3686	4469	3922	7467	7039	4413	4398	5028 ± 1330
c-CH_2CH_2O	4512	3123	4520	5999	4055	6707	4604	5888	4926 ± 1101
NH_2CHO	11075	6456	8927	5886	7307	6103	5854	6311	7240 ± 1735
CH_3CH_2OH	5591	6097	4925	8419	4464	7858	3032	3617	5500 ± 1785
$HCOOH$	7035	5201	6728	7318	6410	6501	7300	6315	6601 ± 642
CH_3OCH_3	4552	3202	5282	6554	2915	3487	2088		4011 ± 1424
CH_3CH_2CN	5282	6185	5605	8386	5113	7504	4885	3471	5804 ± 1448
CH_3NCO	4158	2834	4495	6604	6971	4503	6318	3730	4952 ± 1401
CH_3COCH_3	5170	7603	4936	7534	5263	7581	5796	3517	5925 ± 1412
CH_3CH_2CHO	5150	4393	5581	7178	8680	6876	5585	3797	5905 ± 1490
CH_3COOH	5672	7097	6839	10998	2277	5936	7279	6156	6532 ± 2243
$HCOOCH_3$	4498	4236	4840	7199	7336	6513	2366	3345	5042 ± 1699
$HOCH_2CHO$	8477	10781	5976	4130	11025	5884	6221	3544	7005 ± 2640
$HOCH_2CH_2OH$	15148	9656	6061	9824	4955	8488	6311	5180	8203 ± 3180
CH_3COOCH_3	4923	2794	5373	6121	7516	6972	6036	3719	5432 ± 1488

Figure 5. Summary of the DFT//HF-3c BEs (with ZPE corrections), in K, of the iCOMs on the periodic amorphous water ice model. The first column lists the iCOMs, columns 2–9 present the ZPE-corrected binding energies on different adsorption sites of the amorphous ice model, and column 10 lists the mean BE, along with the standard deviation. The color gradient from gray to black indicates smaller to larger BE values.

B3LYP-D3(BJ). The obtained DFT//HF-3c BE_{ED} values have been compared with those computed at DFT//DFT and ONIOM2, as reported in Figures 4(b) and (c), respectively. The DFT//HF-3c methodology shows a good correlation with both treatments, thereby giving proof of confidence that this DFT//HF-3c scheme can be utilized to obtain accurate BE_{ED} values for the adsorption of iCOMs on water ice surfaces. Interestingly, for some species, more than one optimized structure was identified for optimizations at HF-3c, resulting in different BE_{ED} values (see Table 1). These structures have been illustrated in Figure 9 in Appendix B. In the correlation plot, for the sake of consistency, we only considered the DFT analogous structures.

4.2. Binding Energies on the Amorphous Water Ice Model

The amorphous water ice surface provides a varied selection of adsorption sites, which in turn yields a range of BEs for the studied iCOMs. In this work, eight different adsorption sites were considered according to their H-bonding capabilities (i.e., 1–6 dH as H-bond donors and 7–8 dO as H-bond acceptors; see Figure 2). The starting structures were built by placing the adsorbate close to the dangling atoms of the amorphous surface, following the principle of electrostatic complementarity.

Using the amorphous ice surface, more than 150 adsorption complexes have been optimized. As explained previously, the complexes were first optimized at the HF-3c level and followed by harmonic frequency calculations to validate all the structures as minima, and a scaling factor of 0.863 was applied to the calculated DFT//HF-3c BE_{ED} to derive the corresponding ZPE-corrected BE. Figure 5 reports the BEs of the adsorption of the iCOMs on the different binding sites at the DFT//HF-3c level of theory. The mean BEs are also tabulated, although they should only be considered qualitatively due to the limited sample size of the adsorption sites and thus are not suitable for statistical analysis.

As a trend, the BEs for the adsorption of iCOMs on the crystalline ice surface are higher than the adsorption on amorphous ice. In the former case, the H-bond network extends infinitely throughout the structure, ensuring strong H-bond cooperativity, while in the amorphous ice, the lack of long-range order breaks the H-bond network, which also affects the terminal –OH groups interacting with the adsorbate, hence weakening the H-bond strength. However, in the cavity of the amorphous model, particularly at the dH4 and dH6 binding sites, BEs are comparatively higher due to the formation of multiple H-bonds. Notably, while most BEs for adsorption on amorphous ice fall within the 4000–8000 K range, some reach beyond 10,000 K. This occurs when the nonuniform amorphous surface, due to the ease of rearrangement of the structure, allows adsorbates to interact more closely with the ice, hence increasing the number of H-bonds. Similar to the adsorption on crystalline ice, this effect is particularly pronounced for species containing carboxyl (–COOH), hydroxyl (–OH), and formyl (–CHO) groups, such as CH_3COOH, $HOCH_2CHO$, NH_2CHO, and $HOCH_2CH_2OH$, which form three or more H-bonds with the amorphous

Table 2
Parameters Used to Compute the Desorption Rate Preexponential Factors (in s^{-1}) for the CWS (ν_{CWS}) and ASW (ν_{ASW}) Water Ice Models: Mass of the Molecule (m) in amu, Symmetry Number (σ), Principal Moments of Inertia (I_x, I_y, I_z) in amu · Å^2, Experimental Peak Desorption Temperature (T_{peak}) in K

Species	m	σ	I_x	I_y	I_z	T_{peak}	<BE>	ν_{CWS}	ν_{ASW}	ν_{lit}	Ref
H_2CO	30.03	2	24.40	21.45	2.95	95	4077	1.49×10^{17}	4.77×10^{17}	8.3×10^{16}	1
CH_3NH_2	31.06	1	8.09	38.46	36.97	137	6124	3.02×10^{18}	9.69×10^{18}	4.7×10^{17}	2
CH_3OH	32.04	1	6.55	34.05	35.27	128	5534	2.03×10^{18}	6.52×10^{18}	3.2×10^{17}	1
CH_3CN	41.05	3	5.26	90.59	90.59	120	5271	1.62×10^{18}	5.20×10^{18}	2.4×10^{17}	1
CH_3CHO	44.05	1	14.63	82.60	92.08	100	5028	4.43×10^{18}	1.42×10^{19}	6.5×10^{17}	2
c-CH_2CH_2O	44.05	2	32.88	37.82	59.39	100*	4926	$1.80 \times 10^{18*}$	$5.79 \times 10^{18*}$	…	…
NH_2CHO	45.04	1	11.44	74.16	85.42	176	7240	2.64×10^{19}	8.48×10^{19}	3.7×10^{18}	1
CH_3CH_2OH	46.07	1	23.86	103.30	89.94	169	5500	4.10×10^{19}	1.32×10^{20}	6.5×10^{18}	2
HCOOH	46.03	1	69.67	10.77	80.45	111	6601	4.91×10^{18}	1.58×10^{19}	2.0×10^{18}	2
CH_3OCH_3	46.07	2	21.43	83.87	94.68	101	4011	2.97×10^{18}	9.51×10^{18}	2.0×10^{18}	2
CH_3CH_2CN	55.08	1	30.01	197.79	178.16	119*	5804	$3.14 \times 10^{19*}$	$1.01 \times 10^{20*}$	…	…
CH_3NCO	57.05	1	10.74	197.47	192.01	104	4952	1.26×10^{19}	4.04×10^{19}	6.8×10^{18}	2
CH_3COCH_3	58.08	2	82.55	98.35	170.57	140	5925	3.34×10^{19}	1.07×10^{20}	9.7×10^{18}	2
CH_3CH_2CHO	58.08	1	32.70	200.74	193.57	97	5905	1.77×10^{19}	5.69×10^{19}	8.8×10^{18}	2
CH_3COOH	60.05	1	73.99	88.67	157.48	160	6532	9.53×10^{19}	3.06×10^{20}	1.3×10^{19}	2
$HCOOCH_3$	60.05	1	41.71	122.67	159.10	128	5042	3.87×10^{19}	1.24×10^{20}	4.5×10^{18}	2
$HOCH_2CHO$	60.05	1	21.59	191.93	208.25	160	7005	8.71×10^{19}	2.79×10^{20}	1.4×10^{19}	2
$HOCH_2CH_2OH$	62.07	2	27.48	210.52	227.43	151	8203	4.54×10^{19}	1.46×10^{20}	4.2×10^{19}	2
CH_3COOCH_3	74.08	1	81.90	202.09	273.54	116	5432	7.99×10^{19}	2.56×10^{20}	4.1×10^{19}	2

Note. The mean BE values for the iCOMs on the ASW model are also listed. The preexponential factors obtained from recent literature (ν_{lit}) are listed for comparison. The last column provides references for the T_{peak} and ν_{lit} values taken from the following literature sources: (1) M. Minissale et al. (2022) and (2) N. F. W. Ligterink & M. Minissale (2023). The numbers marked with asterisks (∗) represent estimated T_{peak} values that were used to approximate the preexponential factors.

surface, leading to exceptionally high BEs. In contrast, molecules with ether (–O–) and ester (–COO–) groups, such as c-CH_2CH_2O, CH_3OCH_3, and $HCOOCH_3$, generally exhibit lower BEs due to fewer H-bonding interactions.

4.3. Desorption Rate Preexponential Factors

As described in Section 3.3, the desorption rate preexponential factors, ν_{TST}, have been computed using Equation (6) for all the iCOMs and considering the crystalline water surface (CWS) and the ASW ice models (ν_{CWS} and ν_{ASW}, respectively). The values are reported in Table 2, alongside the input parameters needed to obtain them. The principal moments of inertia have been obtained from the optimized geometries of the molecules using the MOLDRAW program (P. Ugliengo et al. 1993). For the crystalline ice model, the area per adsorbed molecule is 6.36×10^{-19} m^2, while for the amorphous ice model, it is 2.04×10^{-18} m^2. The T_{peak} values have been obtained from M. Minissale et al. (2022) and N. F. W. Ligterink & M. Minissale (2023). They assume submonolayer coverage for the desorption of molecules on different substrates. The T_{peak} listed in Table 2 are for experiments conducted on water ice substrates. The preexponential factors estimated in the aforementioned studies (ν_{lit}) have also been introduced in Table 2 for comparison with the ν_{CWS} and ν_{ASW}.

The calculated preexponential factors range from the order of 10^{17} to 10^{20} with variation across the different species. Between the CWS and ASW models, the preexponential factors differ by a factor of 3, due to the difference in the surface area of the two ice models. For most species, ν_{lit} lies 1 order of magnitude lower than the computed ν_{CWS} values and 2 orders of magnitude lower than the ν_{ASW} ones. This can be attributed to the constant substrate area of 10^{-19} m^2 used in N. F. W. Ligterink & M. Minissale (2023), which is taken as a general assumption. Another difference is the moments of inertia for the adsorbed molecules. In this work, we obtained the values using the MOLDRAW program by first optimizing the molecules using DFT, whereas N. F. W. Ligterink & M. Minissale (2023) determined the moments of inertia using the chemical structures from the ChemSpider database. These differences account for the smaller preexponential factors present in the literature.

5. Discussion

5.1. Comparison with Literature Data

The previous studies available in the literature on the binding energies of iCOMs have been briefly summarized in Section 2. In the following, we compare the binding energies of the iCOMs obtained in this work with those reported in the literature, the values of which are summarized in Table 3. Figure 6 illustrates how the computed BEs in this work compare with theoretical and experimental BE values obtained in the previous works.

5.1.1. Theoretical Works Using Different Ice Models

In the work of M. Lattelais et al. (2011), the binding energies were computed on a periodic water ice surface. The main methodological differences with respect to the present work are (i) the DFT level of theory used, i.e., the pure PW91 method, which neglects the description of the dispersion forces (a serious drawback in view of the dispersion contribution to the BEs, as noted previously); (ii) the water ice surface, which is limited to a crystalline, apolar hexagonal system, hence providing single values; and (iii) ZPE corrections, which were not accounted for. The binding energies computed by V. Wakelam et al. (2017) assume that considering a single water molecule as a representative icy model can give a

Table 3
Comparison of ZPE-corrected BE Values Computed in this Work on the CWS and the Minimum and Maximum Values on the ASW (Min and Max ASW, Respectively) with Theoretical and Experimental Binding Energies Presented in the Literature

Species	BE in This Work			Binding Energies in Literature	
	CWS	Min ASW	Max ASW	Theoretical Data	Experimental Data
H_2CO	5187	3103	6259	2970–3800 (g), 3242 (f), 4500 (a,b)	2050 (e), 3260 ± 60 (d)
CH_3NH_2	7184	4441	8423	…	3900–4500 (p), 5970 (c)
CH_3OH	7385	3809	8709	914–8167 (q), 2344–5331 (g), 4368 (f), 5000 (a,b)	3820 ± 135 (d), 4930 (e)
CH_3CN	6416	2665	7696	3550 (f), 4800 (a)	3790 ± 130 (d), 4680 (e,o)
CH_3CHO	5983	3686	7467	2809–6038 (h), 3192–4603 (i) 3849 (f), 5400 ± 1620 (a,b)	2870 ± 500 (d), 3450–4500 (i), 3800 (e) 4330, 4610 (c), 4650–5850 (h)
c-CH_2CH_2O	5429	3123	6707	…	…
NH_2CHO	8104	5854	11075	2971–6591 (l), 6300 (a)	…
CH_3CH_2OH	5094	3032	8419	3127–7108 (n), 4200, 5500 (a), 6800 (m)	3470 ± 500 (d), 5200 (e), 7880 (c)
HCOOH	8020	5201	7318	3266–8044 (g), 3483 (f) 5382–10559 (j), 5570 (b)	4532 ± 150 (d), 5000 (e)
CH_3OCH_3	4706	2088	6554	4227 (m)	4076 ± 500 (m)
CH_3CH_2CN	6850	3471	8386	…	…
CH_3NCO	4964	2834	6971	2990 ± 1490 (k), 4700 ± 1410 (a,b)	…
CH_3COCH_3	6856	3517	7603	…	3300 ± 500 (d), 5620–6910 (c)
CH_3CH_2CHO	6127	3797	8680	4500 (a)	4500 ± 1350 (d)
CH_3COOH	9184	2277	10998	8152 (m)	6300 ± 500 (d), 7390, 7930 (c)
$HCOOCH_3$	4988	2366	7336	4630 (m)	4000 ± 500(d), 4779 ± 500 (m) 5690–6230 (c)
$HOCH_2CHO$	8386	3544	11025	…	7390 (c)
$HOCH_2CH_2OH$	8424	4955	15148	6326–8419 (l)	…
CH_3COOCH_3	6205	2794	7516	…	…

Note. The data are given in Kelvin. The letters beside the literature values refer to the following sources: (a) V. Wakelam et al. (2017), (b) KIDA database, (c) N. F. W. Ligterink & M. Minissale (2023), (d) E. M. Penteado et al. (2017), (e) UDfA database, (f) A. Das et al. (2018), (g) G. M. Bovolenta et al. (2022), (h) S. Ferrero et al. (2022), (i) G. Molpeceres et al. (2022), (j) S. Ferrero et al. (2020), (k) T. Villadsen et al. (2022), (l) E. Bianchi et al. (2022), (m) M. Lattelais et al. (2011), (n) J. Perrero et al. (2024b), (o) M. P. Collings et al. (2004), (p) H. Chaabouni et al. (2018), and (q) V. Bariosco et al. (2025).

genuine BE value. In this work, with computations at the M06-2X level of theory, neither ZPE nor BSSE corrections were included in the values provided. To address the constraint of employing a singular water molecule to emulate ice, a scaling factor was obtained by fitting the experimental BEs against the computed ones for 16 different species.

In A. Das et al. (2018), some iCOM BEs were computed by simulating the interaction of the species on minimal water ice cluster models of four or six molecules. In E. Bianchi et al. (2022), the BEs of NH_2CHO and $HOCH_2CH_2OH$ were provided using an 18-water cluster model, in which the iCOMs were placed in different binding sites. G. M. Bovolenta et al. (2022) took a different route by showcasing BE distributions, encompassing 225–250 values for 21 interstellar molecules across various amorphous cluster models composed of 22 H_2O molecules. They utilized a three-step computational methodology, which included sampling, geometry optimization at the HF-3 c level, and BE calculation at the DFT level of theory. Average values and standard deviations were derived from a Gaussian fit applied to the set of BEs. V. Bariosco et al. (2025) used a 200 water molecule cluster to obtain a BE distribution for CH_3OH on 223 unique binding sites. All of these studies included ZPE corrections in their calculation.

Certain inferences can be derived from the comparison of these theoretically computed binding energies to the present study. Most of the literature values lie close to the lower bound of BEs obtained in this work. Some values in the theoretical works lie outside the range of computed amorphous BEs, particularly when cluster models of limited sizes are used: In E. Bianchi et al. (2022; using 18 water clusters), the BE ranges of formamide and glycol are relatively shifted to lower values than those computed on our ASW; in A. Das et al. (2018; using 4–6 water clusters), there are multiple instances of lower BEs; in G. M. Bovolenta et al. (2022; using 22 water clusters), several BEs obtained lie lower than the computed range. By using these cluster models to mimic the structure of interstellar water ice, long-range effects such as dispersion forces, H-bond cooperativity, and the consideration of cavity regions are not fully accounted for, which are factors that impart strength to the iCOM/surface interactions and hence the lower values. V. Bariosco et al. (2025) obtained a BE distribution for CH_3OH, with a mean value of 4255 K, a standard deviation of 1558 K, and a whole BE ranging from 914 to 8167 K (that is, including BEs lower than those obtained in the present work). This can be attributed to the presence of a cavity in our amorphous ice model, which generally accounts for higher BEs. Their preexponential factors for methanol are also 1–3 orders of magnitude lower than those calculated in the present work. A key difference lies in the surface area of the model used; V. Bariosco et al. (2025) adopted the standard 10^{-19} m^2, whereas we computed the surface area of the CWS and ASW ice models using the cell parameters. Additionally, the lower preexponential factors in their distribution are likely due to the lower T_{peak} values employed in their calculations. In contrast, we use a single T_{peak} value of 128 K. The binding energies from the most recent theoretical studies have been listed in Table 4 in Appendix C, and the correlation plot comparing them with the mean ASW BEs from this work is presented in Figure 6(a).

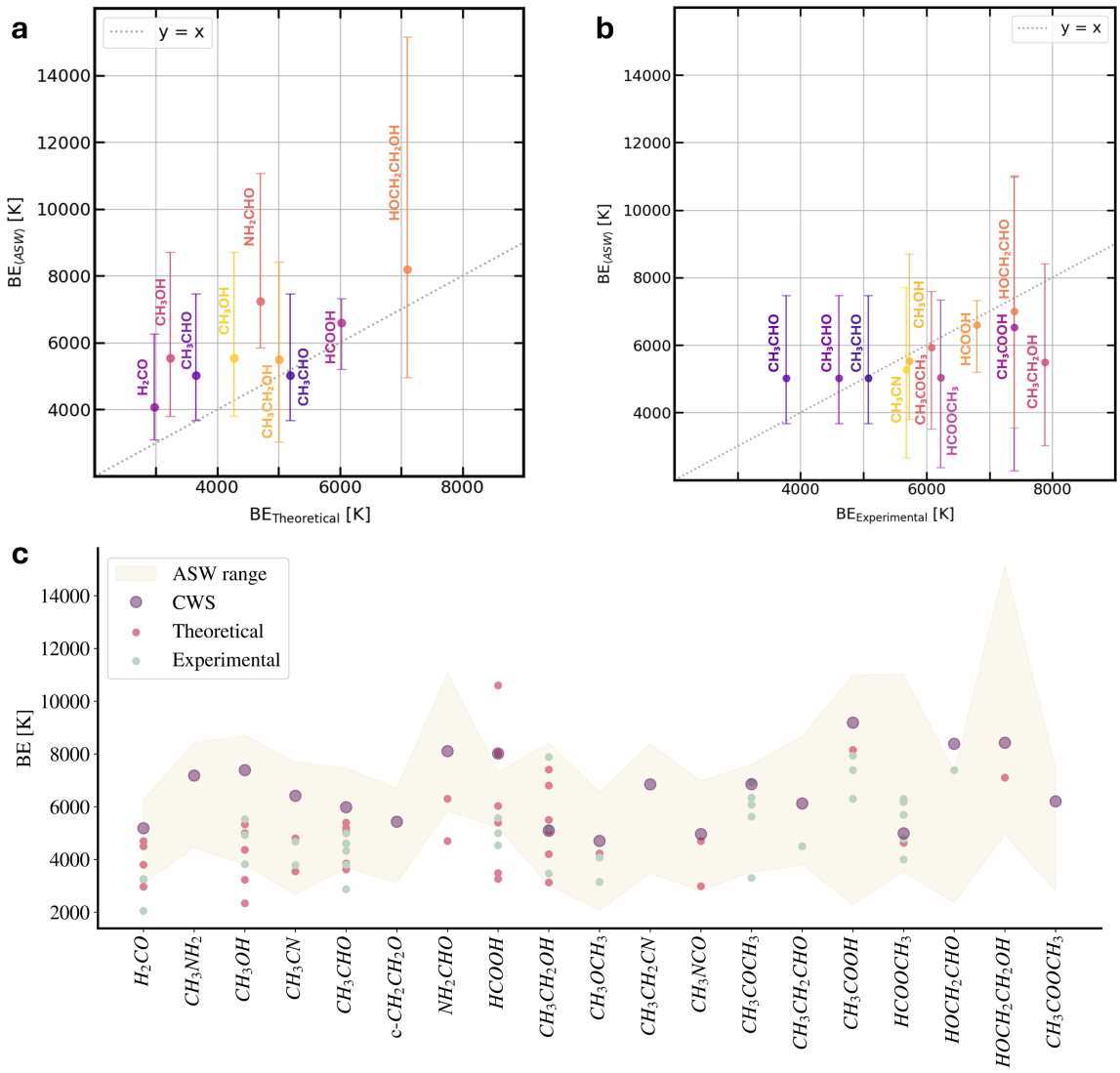

Figure 6. (a) Correlation plot between the ASW BEs range computed in this work for different species and the theoretical binding energies from the recent literature. (b) Correlation plot between the mean ASW BEs computed in this work for different species and experimental binding energies obtained from the recent literature. (c) Comparison of computed and literature BEs. The purple dots mark the BEs on the CWS, while the light-colored range signifies the distribution of BEs (between the minimum and maximum BEs) on the ASW, with both terms computed in this work. The red and green dots represent the literature's theoretical and experimental binding energies, respectively, as listed in Table 3. In plots (a) and (b), the straight line refers to $y = x$ for the sake of comparison with linear correlation. All energies are given in K.

5.1.2. Experimental Works

Experimental derivation of the binding energies involves the TPD technique, which is essentially composed of three sequential steps: (i) preparation of the substrate by condensing water in a phase that closely resembles icy grains observed in the ISM; (ii) exposing the substrate to species adsorption at a very low, constant temperature; and (iii) gradually increasing the substrate temperature through a defined ramp over time to measure the species desorption rate as a function of temperature. Employing appropriate mathematical manipulations of the Polanyi–Wigner equation (K. W. Kolasinski 2012) enables the determination of the binding energies and the desorption rate preexponential factor (ν) from the experimental TPD data (M. Minissale et al. 2022). It is worth noting that TPD experiments do not directly measure the BE of the species but instead measure their desorption enthalpy, which is typically equivalent to the BE if no other activated processes occur (J. He et al. 2016).

In E. M. Penteado et al. (2017), various experimental studies based on TPD measurements were compiled. The aim was to achieve uniformity across different substrates and estimate the BEs using existing data. Recently, N. F. W. Ligterink & M. Minissale (2023) collected and reanalyzed the desorption parameters of different volatile species (including iCOMs) by combining the TST and the Redhead equation to expand the number of molecules for which desorption parameters are available. The TST was used to obtain ν, and the Redhead equation was used to determine the desorption energies by including the calculated ν and TPD experimental values, such as the temperature desorption peak and the heating rate.

Most of the BE estimates reported by N. F. W. Ligterink & M. Minissale (2023) lay within our computed BE range on the ASW ice model. In contrast, some experimental values

obtained from E. M. Penteado et al. (2017) are lower than the computed range. In this work, reported binding energies depend on the experimental desorption temperatures of M. P. Collings et al. (2004) as well as on the BE of H_2O, which is taken to be 4800 K. Since this value is underestimated with respect to our methodology (7200 K reported in S. Ferrero et al. 2020), a much lower estimation of the binding energies was provided. We corrected the BEs in E. M. Penteado et al. (2017) by replacing the BE of H_2O, and the new BE values are listed in Table 5 in Appendix C, along with the most recent experimental works. The correlation plot comparing these BEs to the mean ASW BEs computed in this work is presented in Figure 6(b). With this H_2O "corrected-BE" value, the results compare better with those presented here.

5.1.3. Combined Works and Astrochemical Databases

In combined theoretical and experimental works, S. Ferrero et al. (2022) and G. Molpeceres et al. (2022) focused on the BE of acetaldehyde, highlighting the importance of using a consistent pair of BE and ν values when comparing experiments and computations. The experimental values in the two aforementioned studies lie in the range of ASW BEs computed in this work. The theoretical BE values in S. Ferrero et al. (2022) are comparable to the present study because they used similar methodology and models to simulate the ice surface. The BEs computed in G. Molpeceres et al. (2022) lie toward the lower bound of our range, which can be due to using a different atomistic water ice model (a cluster system consisting of 100 H_2O molecules that was amorphized by means of molecular dynamics simulations) as well as a different quantum mechanical methodology (geometry optimizations and ZPE corrections at the semiempirical GFN2-xTB method and energy refinement at different DFT functionals). Both theoretical and experimental BE values obtained in S. Ferrero et al. (2022) are higher than those obtained in G. Molpeceres et al. (2022), and are more in agreement with the present study.

Additionally, public astrochemical databases such as the Kinetic Database for Astrochemistry (KIDA; V. Wakelam et al. 2012) and UMIST Database for Astrochemistry (UDfA; T. J. Millar et al. 2024) list binding energies for several interstellar and circumstellar species, obtained through theoretical and experimental means from the studies mentioned in the previous sections. Hence, the comparison with the theoretical and experimental works given in the previous sections is valid for the astrochemical databases as well.

As described previously, there is a dearth of literature, particularly regarding the BEs of iCOMs on accurate water ice models, and hence the relevance of this work in providing data on BEs as inputs for astrochemical models for the formation of more complex molecules in interstellar environments. A comparison of the BEs of iCOMs calculated in this work with those that have been discussed previously is presented in Table 3, and a visualization of the same is provided in Figure 6(c).

5.1.4. Theoretical Works Using the Same Ice Models

In prior studies by our group, the BE of a wide range of interstellar species adsorbed on identical ice surface models using the same DFT//HF-3c methodology has been reported. S. Ferrero et al. (2020) performed calculations of the BE of small mixed species encompassing bi- and tri-atomic molecules (H_2, N_2, O_2, CO, CO_2, OCS, HCl, HCN, CH_4, NH_3, H_2O, and H_2S) and radicals (OH, NH_2, HCO, and CH_3). As mentioned previously, the organic compounds (NH_2CHO, H_2CO, HCOOH, CH_3OH, and CH_3CN) have been included in our list of iCOMs in the present work. J. Perrero et al. (2022a) obtained the BE range of 17 S-bearing species, comprising 8 closed-shell species (H_2S, H_2S_2, CS, CH_3SH, SO_2, OCS, H_2CS, and C_3) and 9 radicals (NS, HS, HS_2, HCS, SO, S_2, C_4S, C_2S, and S). Similarly, B. Martínez-Bachs et al. (2024) computed the BE of N-bearing species, including 14 closed-shell molecules (NH_3, HCN, HNC, N_2, HNO, CH_3NH_2, CH_3CN, NH_2CN, HNCO, N_2O, NH_2CHO, HC_3N, CH_2CHCN, and HC_5N) and 7 open-shell species (N, NH, NH_2, CN, NO, OCN, and NO_2). Given the consistent adoption of identical water ice models and computational techniques, a comparative analysis of the BE_{ED} distributions for small mixed molecules, the N-bearing, and S-bearing species with our iCOMs has been performed. It is important to note that only closed-shell species of these previous works are considered in this comparison, since, for radicals, the electronic and dispersive contributions cannot be differentiated due to the different methodology used.

The distribution of BE_{ED} on crystalline and amorphous ice surfaces for the different species is shown in Figure 7. On the crystalline surface, the electronic and dispersion contributions (labeled as "Elec" and "Disp" terms) to the total BE_{ED} values are also illustrated. Several remarks can be made from the trends observed in the plot.

On the crystalline ice surface, the electronic and dispersive contributions show widely different behavior. The values for dispersion interaction present a relatively narrow range, going from lower dispersion of 600 to 3400 K in the case of small mixed species to about 1900–4600 K for S-bearing species, while it ranges between 1500 and 3700 K for N-bearing molecules and 2700–4400 K for iCOMs. The electronic contribution, on the other hand, varies significantly for simple mixed molecules with a broad range from 100–6900 K, whereas it is relatively lower (300–3600 K) for S-containing compounds. This is because volatile species such as H_2O, NH_3, or HCl can form effective H-bonds with the dangling OH of the ice surface, leading to a higher electronic contribution, whereas S-containing molecules have lower nondispersive interactions due to a much lesser extent of H-bonding capabilities. N-bearing species and iCOMs show higher values of electronic contribution, i.e., 500–7000 K and 2800–6500 K, respectively, due to the presence of functional groups that act as H-bond acceptors and donors.

The overall trend for the BE_{ED} of different species on crystalline and amorphous ice models is relatively similar. Small mixed species have smaller BE_{ED} values, and hence they lie at the lower end. S-bearing compounds have a narrower BE_{ED} range, also lying toward the lower end, owing to the lack of nondispersive forces. N-containing molecules and iCOMs, on average, have higher BE_{ED} values than small mixed species and S-bearing species. Generally, the BE_{ED} values on the crystalline ice surface are larger than those on amorphous ice. This is due to the extensive H-bond network in the crystalline model, which leads to an increase in the binding strength. Meanwhile, on the amorphous ice surface, the lack of long-range order reduces the H-bond cooperativity and generally decreases the strength of interactions with the adsorbates.

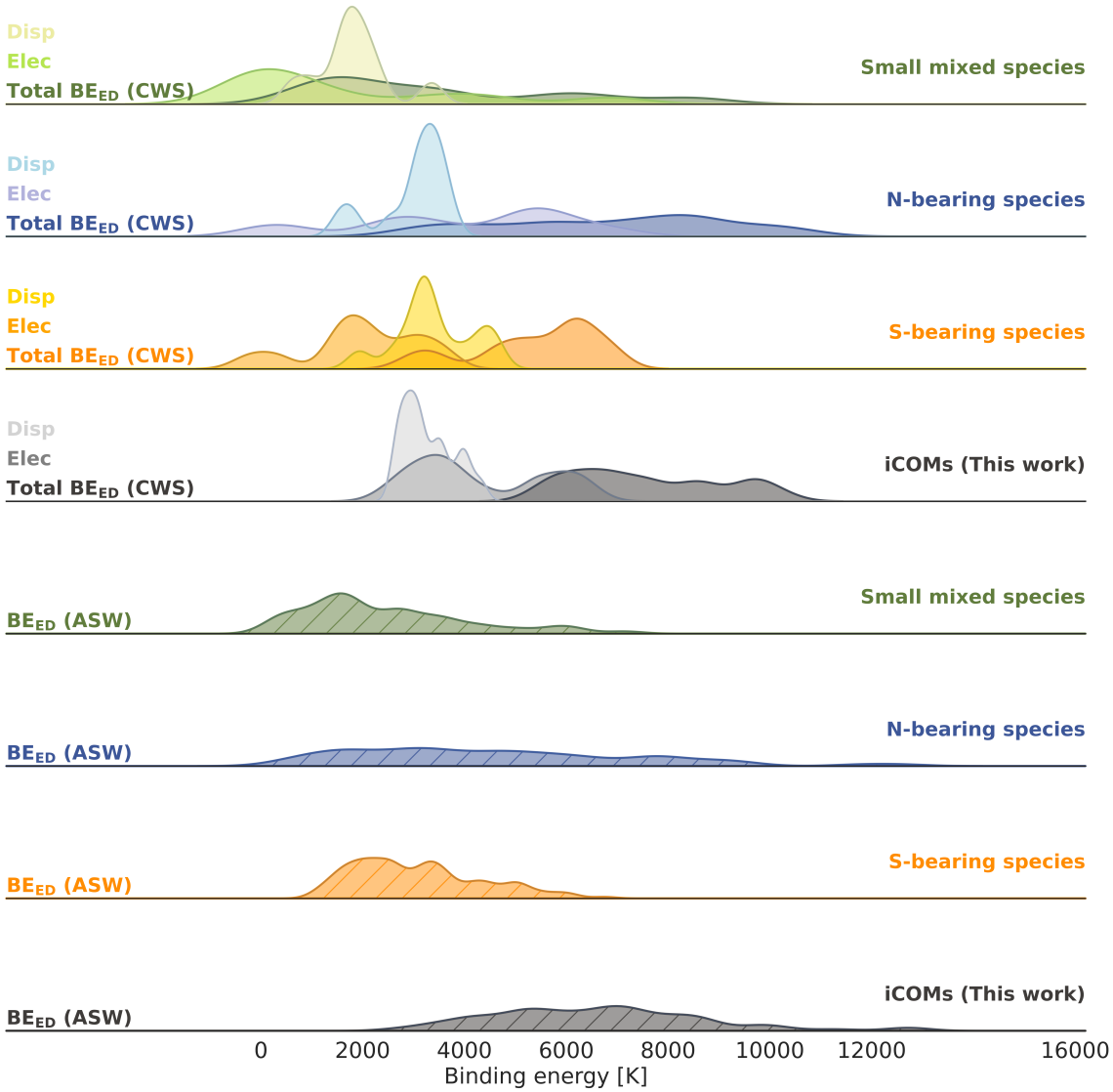

Figure 7. Distribution of BE_{ED} values (in K) computed on the crystalline and amorphous ice models for iCOMs (gray) compared with the small mixed species of S. Ferrero et al. (2020) (green), N-bearing species of B. Martínez-Bachs et al. (2024) (blue), and S-bearing species of J. Perrero et al. (2022a) (orange). The top four plots represent the total BE_{ED} and its components (electronic, Elec; dispersive interactions, Disp) on the crystalline ice surface. The bottom plots indicate the amorphous BE_{ED} values. On the crystalline ice surface, dispersive forces show little variation across species, while electronic forces vary widely depending on the adsorbates' ability to form H-bonds with the ice surface. All the plots, including the components in CWS, are normalized to 1 for comparison.

5.2. Astrophysical Implications

5.2.1. Comparison with Astronomical Observations

Together with the dust temperature, the BEs of iCOMs govern whether they are frozen onto the grain mantles or present in the gas phase, where they can be observed by telescopes. Given the relatively large computed BEs of our sample of iCOMs with respect to water, the dust temperature at which these iCOMs become gaseous is similar or larger than that of water (L. Tinacci et al. 2023), namely around 100 K. These temperatures are present in hot cores and hot corinos (see the introduction at the beginning of this article), which indeed possess the largest iCOM abundances and, consequently, brightest iCOM line intensities. Yet these are relatively small regions, only observable with high spatial resolution interferometers, such as the Atacama Large Millimeter/submillimeter Array (ALMA). Figure 8 shows the temperatures where iCOMs appear in the gas phase around the hot corino NGC1333-IRAS4A, as measured by J. Frediani et al. (2025) via a multiline analysis of ALMA observations of five iCOMs: glycolaldehyde, ethanol, methyl formate, acetaldehyde, and methanol. In the same figure, we report the theoretical dust temperature at which each iCOM is expected to desorb, using the parameters (BEs and preexponential factors) computed in this work. The desorption temperature is given by the lifetime of the species on the dust surface at a given temperature, assuming that the source has an age of 10^4 yr.

The figure shows a reasonable agreement between the two quantities when considering the error bars of the observations and the spread in the calculated BEs. That said, it is important to emphasize that the temperature at which an iCOM appears

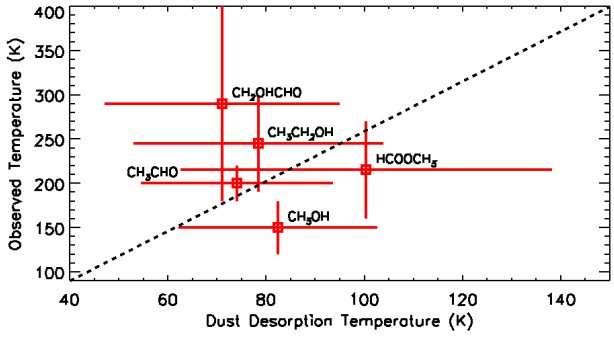

Figure 8. Measured temperatures, with their error bars, at which five iCOMs have been observed in the gas phase by J. Frediani et al. (2025) vs. the theoretical desorption temperatures, calculated using the BE and preexponential factors of this work. The vertical bars show the spread in the computed BE.

in the gas phase also depends on the BE of its precursors, if formed in the gas phase, which may explain the observed temperatures' span in the plot. Needless to say, more observations similar to those of J. Frediani et al. (2025) are needed to assess how realistic the computed BEs are with respect to the processes occurring in the ISM.

5.2.2. The Journey of iCOMs

The journey of iCOMs begins in the hot cores and corinos, i.e., the warm ($\geqslant$100 K) regions of low- and high-mass protostars, respectively. iCOMs may have been synthesized in the previous cold prestellar core period through grain-surface reactions when heavy element-bearing molecules were frozen onto dust grains. The efficiency of surface chemistry increases during the warm-up phase because of the increased diffusion of atoms and radicals on warm grains, producing large terrestrial-like saturated compounds. Species previously frozen in the ice mantles of the molecular clouds may also sublimate into the gas phase, due to the higher core temperature, leading to the formation and detection of more complex molecules. The protostellar phase is thus considered the birthplace of iCOMs.

The gaseous cloud enveloping the protostar dissipates to leave behind a protoplanetary disk, which has a diverse solid-state and gaseous chemical composition consisting of simple as well as complex molecules. If a species exists in the solid state with water ice, it is likely incorporated into icy objects, whereas in the gaseous state, it will contribute toward enriching the giant gaseous planets with the elements contained in the species (K. I. Öberg & E. A. Bergin 2021). Therefore, iCOMs travel through the different phases of stellar evolution to finally be part of comets, asteroids, and planetesimals.

The point where the transition of a species from the solid to the gas phase takes place in the protoplanetary disk is called the "snowline." An efficient way to measure the solid and gaseous content in the protoplanetary disk is to observe where the species disappear from the gas phase as they freeze out onto the water-rich grain mantles—or in other words, to measure their snow lines. Two key parameters determine where the snowline lies: (i) the temperature of the grain and (ii) the BE of the species. In general, the larger the distance from the disk center (and the central protostar), the colder the grains. Therefore, species with lower BEs sublimate to the gas phase at larger disk radii, while molecules with higher BEs are incorporated into the solid grains, which in the case of iCOMs leads to organic content in planetesimals and presolar bodies.

Within this context, it is of interest to compare the calculated BEs of the considered iCOMs with those of water, due to its crucial role in the emergence of life. The idea is to determine which iCOMs are frozen or gaseous within the water snowline. While explicitly modeling iCOM chemistry in a protoplanetary disk is beyond the scope of this work, we can still provide order-of-magnitude estimates regarding which iCOMs are likely to be part of water-enriched planetesimals. As mentioned previously, L. Tinacci et al. (2023) computed the BE distribution on a 200 H_2O amorphous ice model and found that it follows a Gaussian distribution peaked at 4230 K, which was used to estimate the water content of potential planetesimals at varying distances from the disk center. By comparing our BE ranges with Tinacci's BE distribution of water, we find that almost all the iCOMs remain frozen in regions where 96% of water has completely sublimated—namely, where the maximum BE is larger than $\sim$7000 K. This is because most of the iCOMs present exceptionally high BEs and, accordingly, can potentially be inherited directly from the protostellar phase into planetesimals. The only exceptions are H_2CO, CH_3OCH_3, and c-CH_2CH_2O, with maximum BEs lower than $\sim$7000 K (namely, species in which at least a fraction of them is frozen in a region where less than 96% of water is frozen). However, for these species, their maximum BEs are close to this threshold value, and accordingly, some of them can be frozen species and hence also be incorporated into planetesimals and their derivatives, such as comets, meteorites, and protoplanets.

Comets represent the earliest and most primitive material in the solar system and hence provide a perspective into the volatile composition of protoplanetary disks (D. Bockelée-Morvan & N. Biver 2017). iCOMs such as $HOCH_2CH_2OH$, $HCOOCH_3$, HCOOH, and CH_3CHO have been identified in the comet C/1995 O1 (Hale-Bopp) for the first time and later confirmed in several other comets such as C/2012 F6 (Lemmon) and C/2013 R1 (Lovejoy) (D. Bockelée-Morvan et al. 2000; J. Crovisier et al. 2004; N. Biver et al. 2014; L. Le Roy et al. 2015). Comet C/2014 Q2 (Lovejoy) has shown the presence of several species, including iCOMs such as CH_3CH_2OH, $HOCH_2CHO$, $HCOOCH_3$, CH_3CHO, $HOCH_2CH_2OH$, and HCOOH (N. Biver et al. 2015). The 67P/C-G comet was found to contain a set of CO-bearing species like CH_3CHO, CH_3CH_2OH, CH_3COCH_3, CH_3CH_2CHO, HCOOH, CH_3COOH, CH_3COOCH_3, $HOCH_2CHO$, $HOCH_2CH_2OH$, and $HCOOCH_3$ (M. Rubin et al. 2019).

The extent of preservation of these iCOMs in the protoplanetary disk is unclear. On the other hand, the works by E. Bianchi et al. (2019) and M. N. Drozdovskaya et al. (2019) show an impressive correlation between the iCOM abundance measured in (a few) hot corinos and comets, suggesting that iCOMs may have been inherited from the first stages of solar system formation. In the same vein, the analysis of a larger statistical sample of 35 comets and 11 hot corinos by M. Lippi et al. (2024) suggests an inheritance of molecules, including methanol. Finally, C.-F. Lee et al. (2019) and C.-F. Lee et al. (2022) presented similar evidence on a (very small) sample of two protoplanetary disks.

6. Conclusions

In this work, we address an important topic in astrochemistry, i.e., the BEs of iCOMs on interstellar ice surfaces, by means of a computational chemistry approach. The BEs of 19 iCOMs adsorbed on two pure water ice surface models (crystalline and amorphous) have been computed adopting a periodic approach.

The crystalline ice surface imparts a limited variability in the adsorption sites, while the BEs on a realistic amorphous water ice surface provide a wide range of robust and accurate input parameters for numerical astrochemical models to elucidate the chemical evolution of ISM. Moreover, generally, the crystalline BEs were higher compared to the amorphous BE distribution, except for the few exceedingly high values. This is mainly due to the tightly bound H-bond network in the crystalline ice as compared to the amorphous ice.

For several iCOMs, we found BE data in the literature, both computational and experimental studies, as well as in astrochemical databases such as KIDA and UDfA. The ranges of BEs obtained in this work compare well with the literature values, which usually lie in the lower-to-middle regions of the computed amorphous BE distribution. In the previous computational studies, the BE values are relatively lower compared to our work, primarily due to the smaller water clusters used to simulate the interstellar ice model, which miss important dispersion interactions and extensive H-bond networks present in the ices.

From an astrophysical perspective, most of the considered iCOMs present high adsorption BEs on the ice. These adsorbate/ice interactions are stronger than the interactions of water molecules with each other. Therefore, beyond the H_2O snowline of the protoplanetary disks, the accretion of icy materials on dust grains is accompanied by the embedding of organic material in the ice mantle, in the form of these strongly bound iCOMs, which can, with the subsequent agglomeration of dust grains, get inherited directly into planetesimals and, successively, in larger bodies like comets, asteroids, and protoplanets.

Acknowledgments

This project has received funding from the Marie Sklodowska-Curie project "Astro-Chemical Origins" (ACO), grant agreement No. 811312, and within the European Union's Horizon 2020 research and innovation program from the European Research Council (ERC) for the projects "The Dawn of Organic Chemistry" (DOC), grant agreement No. 741002, and "Quantum Chemistry on Interstellar Grains" (QUANTUMGRAIN), grant agreement No. 865657. MICIN (projects PID2021-126427NB-I00 and CNS2023-144902) is also acknowledged. The Italian Space Agency's cofunding of the Life in Space Project (ASI N. 2019-3-U.O) and the Italian Ministry for Universities and Research (MUR; PRIN 2020, Astrochemistry beyond the second period elements, Prot. 2020AFB3FX) are also acknowledged for financial support. Support from Project CH4.0 under the MUR program "Dipartimenti di Eccellenza 2023-2027" (CUP: D13C22003520001) is also acknowledged. The authors gratefully acknowledge the resources provided by Barcelona Supercomputing Center (BSC) in MareNostrum for activities QHS-2022-3-0007 and QHS-2023-2-0011, as well as the supercomputational facilities provided by CSUC. A.R. gratefully acknowledges support through the 2023 ICREA Award. The

atomic coordinates of all the adsorption complexes of iCOMs are available on Zenodo, doi:10.5281/zenodo.15975346.

Appendix A
Computational Details

A.1. Computational Parameters for CRYSTAL17

The computational parameters adopted in S. Ferrero et al. (2020) for optimization and frequency calculations were utilized in this work. To effectively sample reciprocal space, the Pack–Monkhorst mesh was employed (H. J. Monkhorst & J. D. Pack 1976). For crystalline and amorphous ices, a SHRINK factor of 2 was set, resulting in 4 K-points within the first Brillouin zone. The threshold parameters (TOLINTEG) for evaluating Coulomb and exchange bielectronic integrals were set to 7, 7, 7, 7, and 14. Additionally, an integration grid (XLGRID) was incorporated and maintained at default values. These parameters collectively ensure accurate and efficient computational simulations, particularly in characterizing the properties of crystalline and amorphous ices. The Broyden–Fletcher–Goldfarb–Shanno (BFGS) algorithm was adopted for the geometry optimizations (C. G. Broyden 1970; R. Fletcher 1970; D. Goldfarb 1970; D. F. Shanno 1970).

A.2. Details of Binding Energy Calculations

The BEs are computed from the interaction energy between the adsorbed species and the surface according to

$$\Delta E = E_{\mathrm{Complex}} - E_{\mathrm{Ice}} - E_{\mathrm{Species}} \tag{A1}$$

$$\Delta E = E_{(C/C)} - E_{(I/I)} - E_{(S/S)}, \tag{A2}$$

where $E_{(A/B)}$ refers to the energy of A computed on the optimized geometry of B. Therefore, $E_{(C/C)}$ is the energy of the adsorbate/ice complex, $E_{(I/I)}$ is the energy of the ice surface, and $E_{(S/S)}$ stands for the energy of the adsorbed species. This interaction energy does not account for some crucial factors, such as the deformation energy of the ice slab (δE_I), the deformation energy of the adsorbate species (δE_S), and the lateral interaction between the adsorbate molecules of the different replicas of the unit cell (E_L). These terms can be written as

$$\delta E_I = E_{(I/C)} - E_{(I/I)} \tag{A3}$$

$$\delta E_S = E_{(S/C)} - E_{(S/S)} \tag{A4}$$

$$E_L = E_{P_{(S/C)}} - E_{M_{(S/C)}}, \tag{A5}$$

where $E_{P_{(S/C)}}$ and $E_{M_{(S/C)}}$ are the periodic and molecular energy calculations of the adsorbate species on the optimized complex, respectively. Hence, the deformation-free interaction energy (ΔE^*) can be defined as

$$\Delta E^* = E_{(C/C)} - E_{(I/C)} - E_{(S/C)}. \tag{A6}$$

The interaction energy term, which is known as the energy of the complex without the energy of the adsorbate and the energy of the slab, can therefore be defined as the sum of the aforementioned corrections, i.e.,

$$\Delta E = \Delta E^* + \delta E_I + \delta E_S + E_L. \tag{A7}$$

A.2.1. BSSE Correction

Since our computations use a finite basis set of localized Gaussian functions, basis set superposition errors (BSSE) are introduced. To correct the BSSE in the BEs obtained by DFT//DFT and DFT//HF-3c methods, the a posteriori counterpoise (CP) correction (S. Boys & F. Bernardi 1970) is applied, and BE_{ED} (i.e., BE with electronic and dispersion contributions) is the negative of the CP-corrected interaction energies (ΔE^{CP}), i.e.,

$$BE_{ED} = -\Delta E^{CP}, \tag{A8}$$

$$\Delta E^{CP} = \Delta E - BSSE. \tag{A9}$$

A.2.2. ZPE Correction

Zero point energy (ZPE) corrections are evaluated for the BEs according to

$$BE = BE_{ED} - \Delta ZPE. \tag{A10}$$

Each of the terms in Equation (A1) can be corrected for the zero-point vibrational contribution according to the harmonic approximation. Therefore, BE can also be written as

$$BE = E_{Ice} - ZPE_{Ice} + E_{Species} - ZPE_{Species} - [E_{Complex} - ZPE_{Complex}]. \tag{A11}$$

Hence, ΔZPE can be simplified as

$$\Delta ZPE = ZPE_{Complex} - ZPE_{Ice} - ZPE_{Species}. \tag{A12}$$

In this work, the ΔZPE has only been computed for the crystalline complexes, and the scaling factor obtained in Figure 3 is used to correct the amorphous BEs.

Appendix B
Crystalline Adsorption Geometries

The different adsorption geometries of the iCOMs on the crystalline ice surface are presented in Figure 9.

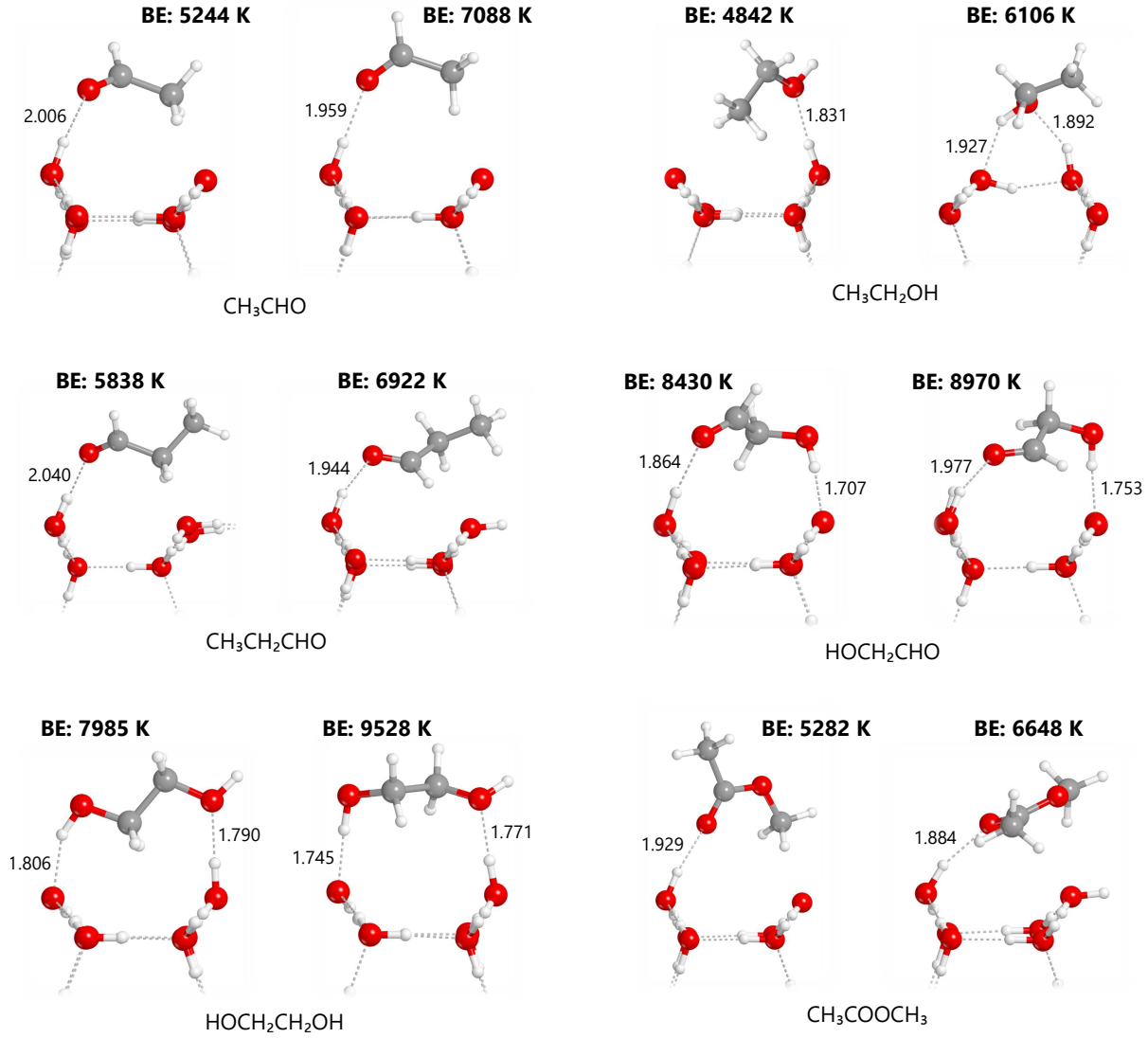

Figure 9. Different adsorption geometries for CH_3CHO, CH_3CH_2OH, CH_3CH_2CHO, $HOCH_2CHO$, $HOCH_2CH_2OH$, and CH_3COOCH_3 at the HF-3c level of theory. The two structures differ in the orientation of the adsorbed species on the ice model, the number of H-bonds formed between the adsorbate and ice surface, as well as the H-bond lengths. The two BEs obtained for each species using DFT//HF-3c are also listed in Table 1. The H-bond lengths are given in Å and the BEs are given in Kelvin.

Appendix C
Data for Comparison with Theoretical and Experimental Studies

The BE values computed in this work on the ASW ice surface have been compared with theoretical literature values in Table 4, and with experimental literature values in Table 5.

Table 4
Comparison of ASW BEs Computed in This Work (Mean, Minimum, and Maximum Values, Respectively) with the Theoretical Binding Energies Obtained from Recent Literature (Recommended, Minimum, and Maximum Values, Respectively)

Species	BE in This Work			Theoretical Binding Energies			References
	<ASW>	Min ASW	Max ASW	Rec BE	Min BE	Max BE	
H_2CO	4077	3103	6259	2970	2668	3272	(1)
CH_3OH	5534	3809	8709	3235	2533	3937	(1)
CH_3OH	5534	3809	8709	4255	914	8167	(2)
CH_3CHO	5028	3686	7467	5194	2809	6038	(3)
CH_3CHO	5028	3686	7467	3646	3192	4603	(4)
NH_2CHO	7240	5854	11075	4700	2971	6591	(5)
CH_3CH_2OH	5500	3032	8419	5006	3127	7108	(6)
HCOOH	6601	5201	7318	6027	5225	6829	(1)
$HOCH_2CH_2OH$	8203	4955	15148	7100	6326	8419	(5)

Note. All values are given in K. The references in the last column correspond to the following sources: (1) G. M. Bovolenta et al. (2022), (2) V. Bariosco et al. (2025), (3) S. Ferrero et al. (2022), (4) G. Molpeceres et al. (2022), (5) E. Bianchi et al. (2022), and (6) J. Perrero et al. (2024b).

Table 5
Comparison of ASW BEs Computed in this Work (Mean, Minimum, and Maximum Values, Respectively) with the Experimental Binding Energies Obtained from Recent Literature

Species	BE in This Work			Experimental BE	References
	<ASW>	Min ASW	Max ASW		
CH_3OH	5534	3809	8709	5730	(1)
CH_3CN	5271	2665	7696	5685	(1)
CH_3CHO	5028	3686	7467	3774	(2)
CH_3CHO	5028	3686	7467	4610	(3)
CH_3CHO	5028	3686	7467	5080	(4)
CH_3CH_2OH	5500	3032	8419	7880	(3)
HCOOH	6601	5201	7318	6798	(1)
CH_3COCH_3	5925	3517	7603	6080	(3)
CH_3COOH	6532	2277	10998	7390	(3)
$HCOOCH_3$	5042	2366	7336	6230	(3)
$HOCH_2CHO$	7005	3544	11025	7390	(3)

Note. All values are given in K. The references in the last column correspond to the following sources: (1) Corrected E. M. Penteado et al. (2017) BEs using 7200 K as BE of H_2O, with TPD data originally taken from M. P. Collings et al. (2004), (2) G. Molpeceres et al. (2022), (3) N. F. W. Ligterink & M. Minissale (2023), and (4) S. Ferrero et al. (2022).

ORCID iDs

Harjasnoor Kakkar https://orcid.org/0000-0002-8984-2356
Berta Martínez-Bachs https://orcid.org/0000-0002-1290-7019
Cecilia Ceccarelli https://orcid.org/0000-0001-9664-6292
Piero Ugliengo https://orcid.org/0000-0001-8886-9832
Albert Rimola https://orcid.org/0000-0002-9637-4554

References

Agúndez, M., Molpeceres, G., Cabezas, C., et al. 2025, A&A, 693, L20
Arce, H. G., Santiago-García, J., Jørgensen, J. K., Tafalla, M., & Bachiller, R. 2008, ApJL, 681, L21
Bachiller, R., Codella, C., Colomer, F., Liechti, S., & Walmsley, C. M. 1998, A&A, 335, 266
Bachiller, R., Liechti, S., Walmsley, C. M., & Colomer, F. 1995, A&A, 295, L51
Bacmann, A., Taquet, V., Faure, A., Kahane, C., & Ceccarelli, C. 2012, A&A, 541, L12
Bariosco, V., Pantaleone, S., Ceccarelli, C., et al. 2024, MNRAS, 531, 1371
Bariosco, V., Tinacci, L., Pantaleone, S., et al. 2025, MNRAS, 539, 82
Becke, A. D. 1993, JChPh, 98, 1372
Behmard, A., Fayolle, E. C., Graninger, D. M., et al. 2019, ApJ, 875, 73
Belloche, A., Maury, A. J., Maret, S., et al. 2020, A&A, 635, A198
Bertin, M., Doronin, M., Michaut, X., et al. 2017, A&A, 608, A50
Bertin, M., Romanzin, C., Michaut, X., Jeseck, P., & Fillion, J.-H. 2011, JPCC, 115, 12920
Bianchi, E., Codella, C., Ceccarelli, C., et al. 2019, MNRAS, 483, 1850
Bianchi, E., Chandler, C. J., Ceccarelli, C., et al. 2020, MNRAS, 498, L87
Bianchi, E., López-Sepulcre, A., Ceccarelli, C., et al. 2022, ApJL, 928, L3
Bianchi, E., Remijan, A., Codella, C., et al. 2023, ApJ, 944, 208
Biver, N., Bockelée-Morvan, D., Debout, V., et al. 2014, A&A, 566, L5
Biver, N., Bockelée-Morvan, D., Moreno, R., et al. 2015, SciA, 1, e1500863
Blake, G. A., Sutton, E. C., Masson, C. R., & Phillips, T. G. 1987, ApJ, 315, 621
Bockelée-Morvan, D., & Biver, N. 2017, RSPTA, 375, 20160252
Bockelée-Morvan, D., Lis, D. C., Wink, J. E., et al. 2000, A&A, 353, 1101
Boogert, A. A., Gerakines, P. A., & Whittet, D. C. 2015, ARA&A, 53, 541
Bovolenta, G. M., Vogt-Geisse, S., Bovino, S., & Grassi, T. 2022, ApJS, 262, 17
Boys, S., & Bernardi, F. 1970, MolPh, 19, 553
Broyden, C. G. 1970, JApMa, 6, 76
Bulik, A., Martínez-Bachs, B., Bancone, N., et al. 2025, PCCP, 27, 11907
Burke, D. J., Puletti, F., Brown, W. A., et al. 2014, MNRAS, 447, 1444
Cazaux, S., Tielens, A. G. G. M., Ceccarelli, C., et al. 2003, ApJL, 593, L51
Ceccarelli, C., Caselli, P., Fontani, F., et al. 2017, ApJ, 850, 176
Ceccarelli, C., Codella, C., Balucani, N., et al. 2023, in ASP Conf. Ser. 534, Protostars and Planets VII, ed. S. Inutsuka et al. (San Francisco, CA: ASP), 379
Cernicharo, J., Agúndez, M., Cabezas, C., et al. 2021, A&A, 649, L15
Cernicharo, J., Marcelino, N., Roueff, E., et al. 2012, ApJL, 759, L43
Chaabouni, H., Diana, S., Nguyen, T., & Dulieu, F. 2018, A&A, 612, A47
Civalleri, B., Doll, K., & Zicovich-Wilson, C. M. 2007, JPCB, 111, 26
Codella, C., Ceccarelli, C., Caselli, P., et al. 2017, A&A, 605, L3
Collings, M. P., Anderson, M. A., Chen, R., et al. 2004, MNRAS, 354, 1133
Collings, M. P., Frankland, V., Lasne, J., et al. 2015, MNRAS, 449, 1826
Crovisier, J., Bockelée-Morvan, D., Biver, N., et al. 2004, A&A, 418, L35
Dapprich, S., Komáromi, I., Byun, K., Morokuma, K., & Frisch, M. J. 1999, JMoSt, 461–462, 1
Das, A., Sil, M., Gorai, P., Chakrabarti, S. K., & Loison, J. C. 2018, ApJS, 237, 9
Dovesi, R., Erba, A., Orlando, R., et al. 2018, WIREs Comput. Mol. Sci., 8, e1360
Drozdovskaya, M. N., van Dishoeck, E. F., Rubin, M., Jørgensen, J. K., & Altwegg, K. 2019, MNRAS, 490, 50
Duflot, D., Toubin, C., & Monnerville, M. 2021, FrASS, 8, 24
Dunning, T. H. J. 1989, JChPh, 90, 1007
Endres, C. P., Schlemmer, S., Schilke, P., Stutzki, J., & Müller, H. S. 2016, JMoSp, 327, 95
Enrique-Romero, J., Rimola, A., Ceccarelli, C., et al. 2022, ApJS, 259, 39
Ferrero, S., Ceccarelli, C., Ugliengo, P., Sodupe, M., & Rimola, A. 2023a, ApJ, 951, 150
Ferrero, S., Ceccarelli, C., Ugliengo, P., Sodupe, M., & Rimola, A. 2024, ApJ, 960, 22
Ferrero, S., Grieco, F., Ibrahim, M. A.-S., et al. 2022, MNRAS, 516, 2586
Ferrero, S., Pantaleone, S., Ceccarelli, C., et al. 2023b, ApJ, 944, 142
Ferrero, S., Zamirri, L., Ceccarelli, C., et al. 2020, ApJ, 904, 11
Fletcher, R. 1970, CompJ, 13, 317
Fraser, H. J., Collings, M. P., Dever, J. W., & McCoustra, M. R. S. 2004, MNRAS, 353, 59
Frediani, J., De Simone, M., Testi, L., et al. 2025, A&A, 695, A78
Frisch, M. J., Trucks, G. W., Schlegel, H. B., et al. 2016, Gaussian~16 Revision C.01 (Wallingford, CT: Gaussian Inc.)
Germain, A., Tinacci, L., Pantaleone, S., Ceccarelli, C., & Ugliengo, P. 2022, ESC, 6, 1286
Goldfarb, D. 1970, MaCom, 24, 23
Grimme, S. 2011, WIREs Comput. Mol. Sci., 1, 211
Grimme, S., Antony, J., Ehrlich, S., & Krieg, H. 2010, JChPh, 132, 154104
Groyne, M., Champagne, B., Baijot, C., & De Becker, M. 2025, A&A, 698, A284
Hama, T., & Watanabe, N. 2013, ChRv, 113, 8783
He, J., Acharyya, K., & Vidali, G. 2016, ApJ, 825, 89
Herbst, E., & van Dishoeck, E. F. 2009, ARA&A, 47, 427
Jones, A. P. 2016, RSOS, 3, 160224
Jones, A. P., Köhler, M., Ysard, N., Bocchio, M., & Verstraete, L. 2017, A&A, 602, A46
Kaur, H., Wang, W., Pérez-Ríos, J., et al. 2025, ESC, 9, 1724
King, D. A. 1975, SurSc, 47, 384
Kolasinski, K. W. 2012, Surface Science: Foundations of Catalysis and Nanoscience (New York: Wiley)
Kruse, H., & Grimme, S. 2012, JChPh, 136, 154101
Lattelais, M., et al. 2011, A&A, 532, A12
Le Roy, L., Altwegg, K., Balsiger, H., et al. 2015, A&A, 583, A1
Lee, C., Yang, W., & Parr, R. G. 1988, PhRvB, 37, 785
Lee, C.-F., Codella, C., Ceccarelli, C., & López-Sepulcre, A. 2022, ApJ, 937, 10
Lee, C.-F., Codella, C., Li, Z.-Y., & Liu, S.-Y. 2019, ApJ, 876, 63
Lee, J.-E., Baek, G., Lee, S., et al. 2023, ApJ, 956, 43
Lefloch, B., Ceccarelli, C., Codella, C., et al. 2017, MNRAS, 469, L73
Ligterink, N. F. W., & Minissale, M. 2023, A&A, 676, A80
Lippi, M., Podio, L., Codella, C., et al. 2024, ApJL, 970, L5
López-Sepulcre, A., Codella, C., Ceccarelli, C., Podio, L., & Robuschi, J. 2024, A&A, 692, A120
López-Sepulcre, A., Sakai, N., Neri, R., et al. 2017, A&A, 606, A121
Luna, R., Millán, C., Domingo, M., Santonja, C., & Satorre, M. 2015, Vacuu, 122, 154
Maldoni, M. M., Egan, M. P., Smith, R. G., Robinson, G., & Wright, C. M. 2003, MNRAS, 345, 912
Manigand, S., Jørgensen, J. K., Calcutt, H., et al. 2020, A&A, 635, A48
Martínez-Bachs, B., Ferrero, S., Ceccarelli, C., Ugliengo, P., & Rimola, A. 2024, A&A, 969, 63
McClure, M. K., Rocha, W. R. M., Pontoppidan, K. M., et al. 2023, NatAs, 7, 431
McGuire, B. A. 2022, ApJS, 259, 30
McKellar, A. 1940, PASP, 52, 187
Millar, T. J., Walsh, C., Van de Sande, M., & Markwick, A. J. 2024, A&A, 682, A109
Minissale, M., Aikawa, Y., Bergin, E., et al. 2022, ESC, 6, 597
Molinari, S., Ceccarelli, C., White, G. J., et al. 1999, ApJ, 521, L71
Molpeceres, G., & Kästner, J. 2021, ApJ, 910, 55
Molpeceres, G., Kästner, J., Herrero, V. J., Peláez, R. J., & Maté, B. 2022, A&A, 664, A169
Molpeceres, G., Tsuge, M., Furuya, K., et al. 2024, JPCA, 128, 3874
Molpeceres, G., Zaverkin, V., Furuya, K., Aikawa, Y., & Kästner, J. 2023, A&A, 673, A51
Monkhorst, H. J., & Pack, J. D. 1976, PhRvB, 13, 5188
Nazari, P., van Gelder, M. L., van Dishoeck, E. F., et al. 2021, A&A, 650, A150
Öberg, K. I., & Bergin, E. A. 2021, PhR, 893, 1
Pantaleone, S., Enrique-Romero, J., Ceccarelli, C., et al. 2020, ApJ, 897, 56
Pantaleone, S., Enrique-Romero, J., Ceccarelli, C., et al. 2021, ApJ, 917, 49
Papajak, E., Zheng, J., Xu, X., Leverentz, H. R., & Truhlar, D. G. 2011, JCTC, 7, 3027
Pascale, F., Zicovich-Wilson, C. M., López Gejo, F., et al. 2004, JCoCh, 25, 888
Penteado, E. M., Walsh, C., & Cuppen, H. M. 2017, ApJ, 844, 71
Perrero, J., Beitia-Antero, L., Fuente, A., Ugliengo, P., & Rimola, A. 2024a, ApJ, 971, 36
Perrero, J., Enrique-Romero, J., Ferrero, S., et al. 2022a, ApJ, 938, 158
Perrero, J., Enrique-Romero, J., Martínez-Bachs, B., et al. 2022b, ESC, 6, 496

Perrero, J., Vitorino, J., Congiu, E., et al. 2024b, PCCP, 26, 18205
Polanyi, M., & Wigner, E. 1925, EPJA, 33, 429
Rakić, V., & Damjanović, L. 2013, Temperature-Programmed Desorption (TPD) Methods (Berlin: Springer), 131
Redhead, P. 1962, Vacuu, 12, 203
Rimola, A., Skouteris, D., Balucani, N., et al. 2018, ESC, 2, 720
Rocha, W. R. M., van Dishoeck, E. F., Ressler, M. E., et al. 2024, A&A, 683, A124
Rubin, M., Bekaert, D. V., Broadley, M. W., Drozdovskaya, M. N., & Wampfler, S. F. 2019, ESC, 3, 1792
Salter, T. L., Stubbing, J. W., Brigham, L., & Brown, W. A. 2018, JChPh, 149, 164705
Sameera, W. M. C., Senevirathne, B., Andersson, S., Maseras, F., & Nyman, G. 2017, The Journal of Physical Chemistry C, 121, 15223
Schaff, J. E., & Roberts, J. T. 1998, Langmuir, 14, 1478
Schmid, M., Parkinson, G. S., & Diebold, U. 2023, ACS Phys. Chem. Au., 3, 44
Schäfer, A., Horn, H., & Ahlrichs, R. 1992, JChPh, 97, 2571
Scibelli, S., & Shirley, Y. 2020, ApJ, 891, 73
Shanno, D. F. 1970, MaCom, 24, 647
Sure, R., & Grimme, S. 2013, JCoCh, 34, 1672
Swings, P., & Rosenfeld, L. 1937, ApJ, 86, 483
Tait, S. L., Dohnálek, Z., Campbell, C. T., & Kay, B. D. 2005, JChPh, 122, 164708
Taquet, V., López-Sepulcre, A., Ceccarelli, C., et al. 2015, ApJ, 804, 81
Tatewaki, H., & Huzinaga, S. 1980, JCoCh, 1, 205
Tinacci, L., Germain, A., Pantaleone, S., et al. 2022, ESC, 6, 1514
Tinacci, L., Germain, A., Pantaleone, S., et al. 2023, ApJ, 951, 32
Ugliengo, P., Viterbo, D., & Chiari, G. 1993, Zeitschrift für Kristallographie—Crystalline Materials, 207, 9
van Gelder, M. L., Tabone, B., Tychoniec, L., et al. 2020, A&A, 639, A87
Villadsen, T., Ligterink, N. F. W., & Andersen, M. 2022, A&A, 666, A45
Wakelam, V., Herbst, E., Loison, J.-C., et al. 2012, ApJS, 199, 21
Wakelam, V., Loison, J.-C., Mereau, R., & Ruaud, M. 2017, MolAs, 6, 22
Watanabe, N., & Kouchi, A. 2008, PrSS, 83, 439
Wenzel, G., Gong, S., Xue, C., et al. 2025, ApJL, 984, L36
Zamirri, L., Ugliengo, P., Ceccarelli, C., & Rimola, A. 2019, ESC, 3, 1499
Zicovich-Wilson, C. M., Pascale, F., Roetti, C., et al. 2004, JCoCh, 25, 1873